Assessment of Numerical Modelling for Steady State Jet Impingement Cooling in Different Geometries

Rouzbeh Ghazihesami

A Thesis

in

The Department of Mechanical and Industrial Engineering

Presented in Partial Fulfillment of the Requirements

For the Degree of Master of Applied Science in Mechanical Engineering

Concordia University

Montreal, Quebec, Canada

November 2015

Concordia University

School of Graduate Studies

This is to certify that the thesis prepared

By: Rouzbeh Ghazihesami

Entitled: Assessment of Numerical Modelling for Steady State Jet Impingement Cooling in Different Geometries

and submitted in partial fulfillment of the requirements of the degree of

Master of Applied Science (Mechanical Engineering)

complies with the regulations of the University and meets the accepted standards with respect to originality and quality.

Signed by the final examining committee:

Dr Charles B Kiyanda Chair

Dr Nizar Bouguila Examiner

Dr Lyes Kadem Examiner

Dr Hoi Dick Ng Supervisor

Approved by

Chair of Department or Graduate Program Director

Date Dean of Faculty

ABSTRACT

Assessment of Numerical Modelling for Steady State Jet Impingement Cooling in Different Geometries

Rouzbeh Ghazihesami

Concordia University, 2015

In this thesis, the suitability of CFD to evaluate and predict physical phenomena in lieu of experimental work in a jet impingement application is assessed. Previous experimental work looked at the effectiveness of different geometries in improving jet impingement cooling. This work was used to construct a numerical model of two of the geometries each running at three different Reynolds numbers. First a turbulence model is selected based on a simple 2D axisymmetric jet impingement case. The *k-ω* SST model produced the most accurate results and was thus selected. The model was then used to simulate jet impingement in both a basic flatplate and a corrugated geometry. The corrugated geometry was expected to improve cooling performance. The trend was seen in the numerical results, particularly at higher velocities and at the most downstream jets. The trend replicates that of the experimental results, with negligible impact of the corrugations before the 3-4th jet.

ACKNOWLEDGMENTS

I have been supported tremendously throughout the length of this research by my supervisor Dr Ng, whom I cannot thank enough. He was extremely patient throughout all the issues and difficulties I encountered and gave me the freedom to guide this work. I have learnt an immense amount in this process and for that I will be forever grateful.

I have to thank my brother for his help throughout this research. He helped me settle in this city when I first arrived and knew no one, and introduced me to many groups and people who've made my life richer and happier as a result. I've learnt a great deal about the field of CFD and become a more rounded engineer as a result and his help was instrumental.

My parents have provided me with their endless love and support throughout this work. They had the foresight to send me abroad from a young age so that I could learn about new people, cultures, languages and experiences. This work is only one of the fruits of all that labor and though it is a debt I can never repay, I am eternally grateful for all that they gave me.

I'd like to thank Dr Pierre Gauthier and Rolls Royce for taking a chance on me and giving me the opportunity to learn about a new field and enriching my knowledge and skillset in the process.

To all the amazing people and friends that I made in this unique city of Montreal, thank you for being there and helping me grow as a person. I have learned a great deal about life and who I want to be because of your support.

CONTENTS

LIST OF FIGURES

NOMENCLATURE

z	Jet impingement height
x	Jet streamwise distance
y	Jet spanwise distance
L	Characteristic distance
h	Convective heat transfer coefficient
k	Conductive heat transfer coefficient
T_∞	Freestream temperature
T_w	Wall temperature
q	Heat flux
ρ	Density
d	Jet/Inlet diameter
μ	Dynamic viscosity
τ_w	Wall shear stress
CFD	Computational Fluid Dynamics
Re	Reynolds number
Nu	Nusselt number
Pr	Prandtl Number
GCI	Grid Convergence Index

Chapter 1. INTRODUCTION

Gas turbine development has come a long way since the first turbine was patented in 1791 by John Barber and the first tests began early in the 20th century. Gas turbines now power a variety of devices, most commonly in aviation and utility power applications. Gas turbines must operate under extraordinary conditions under different usage cycles. For aircraft, the gas turbine must be able to respond during high load takeoff applications as well as high altitude cruises. Improving fuel efficiency and reducing emissions has become one of the key objectives of engine design. One of the key ways to improving engine efficiency is increasing turbine inlet temperature. Most gas turbines operate with turbine inlet temperatures of ≈1400-1500°C and new models are approaching 2000°C [1, 2], which can be very near to both combustion chamber and blade materials' melting points. Cooling air is generally directed to the gas turbine hot sections from the compressor at temperatures near to 600°C requiring heat flux values on the order of 1MW [3]. Cooling air can however, interfere with the combustion flow and reduce engine efficiency. In order to operate the material at such temperatures and minimize cooling air flow and associated penalties, advanced cooling techniques are employed. Some of these include convection cooling, impingement cooling, film cooling and transpiration (effusion) cooling. A brief overview of each technique is given below.

Convection cooling is an internal cooling technique whereby air is taken through the root of a turbine blade and to the tip through passages in the blade body. The material is heated from the outside and cooled by passage of the air through the inside. It is therefore desirable that the maximum surface area be available for the air to pass through, resulting in mazelike structures in the blade.

Film cooling is the process of injecting a layer of cooling air into the boundary layer of the working fluid. The air acts as an insulating layer between the solid from which the air exits and the hot chamber into which it flows.

Transpiration cooling occurs by flow of coolant through a porous wall so the material cools as the coolant flows through it and also forms a layer of cool air in the boundary layer in the high temperature region similar to film cooling. Transpiration cooling results in a more even temperature profile across the surface than film cooling, reducing thermal stresses as well as coolant flow requirements [4].

Effusion cooling requires the drilling of a large number of small holes through which the coolant can pass. It does not suffer the structural disadvantages of using a porous wall and offers better thermal protection than film cooling [5]. This is due to the fact that film cooling often requires a high amount of coolant, which can then generate vortices and mix with the hot gas flow, reducing efficiency. The lower amount of cooling required and the lower velocities at which the coolant can be discharged result in minimal impact on the hot gas flow. Due to manufacturing and modeling difficulties however, effusion cooling has not so far been commercially exploited to a significant degree, though its use on combustor liners is nearer than in turbine blades [6].

Lastly, **impingement cooling** is an internal cooling technique whereby coolant jet is directed at the surface to be cooled. It is one of the most effective cooling techniques available and is thus used where thermal loads are highest [2]. Its use spans applications as diverse as gas turbines, industrial scale boiled eggs as

well as metal and glass cooling. This paper will focus on this form of cooling. A graphic representation of the above cooling methods can be seen in Figure 1.1.

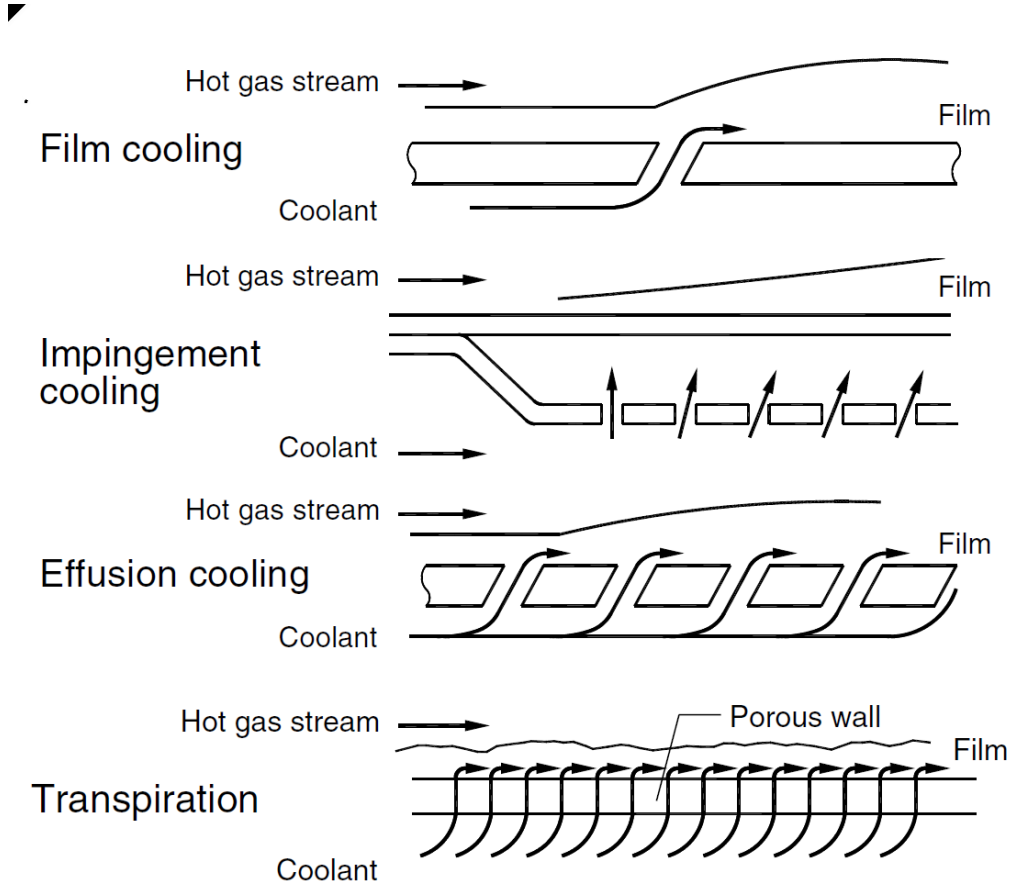

Figure 1.1 – Different combustor/blade cooling methods [7]

1.1 Jet Impingement Basics

It is the aim of any cooling system to minimize the amount of flow required, since any flow used for cooling is not being used in the combustion chamber where it could be producing work. In this respect, jet impingement is preferable to film cooling which can require significantly greater amounts of cooling and at a greater cost due to interactions with the hot gas. Jet impingement is therefore one of the most

effective internal cooling techniques available. A turbulent jet is discharged onto a solid surface removing heat from that surface. Jet impingement may be up to a magnitude of 10^2 more efficient with coolant flow than other methods like convection and film cooling due in part to the thin boundary layer of the flow as well as entrainment of surrounding gases by the spent impingement eddies [8]. A certain amount of air is directed from the compressor of a gas turbine engine to high temperature areas of the engine. The jet impingement setup consists of one high pressure area where the air is directed from the compressor, a slotted plate and the impingement surface. A turbulent high Reynolds number jet is discharged through the slotted plate onto the impingement surface, carrying heat away from the surface. A variety of nozzle geometries can be used, though circular nozzles have higher performance characteristics than slot/rectangular nozzles, hence their more common usage [9]. Jet impingement in gas turbines is used primarily on the turbine guide vane as well as the combustion chamber lining. A schematic showing the velocity profile of an impingement jet is provided in Figure 1.2.

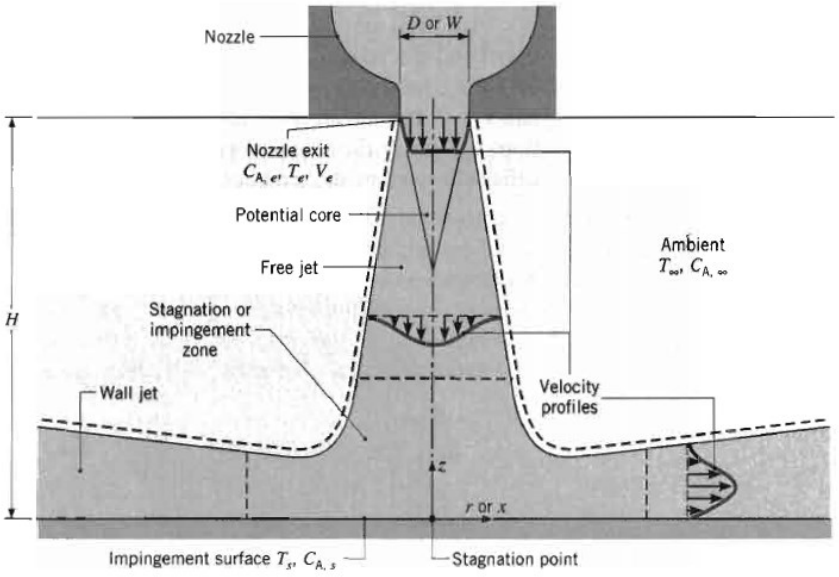

Figure 1.2 – Profile of an impingement jet [2]

As the jet is discharged, it changes from a uniform velocity profile at the nozzle to a fully developed profile further downfield (the extent depends on the distance between the jet exit and the plate). The potential core of the jet, where the uniform velocity is maintained, contracts as momentum transfer between the jet and the surrounding low momentum air takes place (seen in Figure 1.3). This core area has been found to be much bigger in round nozzle discharged jets than other orifice geometries, hence the higher effectiveness of circular nozzles to other geometries. This core reduction causes the average velocity of the jet to decrease as plate distance to the nozzle increases. Figure 1.3 shows the jet profile as it develops at higher height/diameter ratios (*z/d*).

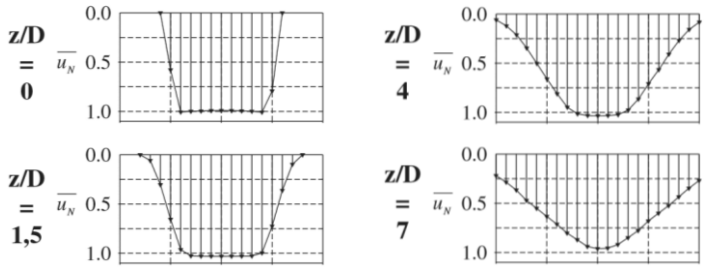

Figure 1.3 – Example of velocity profile development at z/D distance from nozzle [10]

The flow decelerates as it approaches the wall until its velocity becomes negative and reverses direction. This is the stagnation region and the local properties of the fluid may be substantially different from a non-stagnating flow. Turbulence is seen to be higher in this region which may occupy approximately 1.2 nozzle diameters above the wall in round diameter jets [11].

Another phenomenon that arises from an array of impingement holes is the upwash or 'fountain'. Once jets from two adjacent impingement holes impinge on the surface, they enter the wall jet phase. As the two opposing wall jets collide, they form a jet of air that rises up. Slayzak et al. [12] performed an experimental analysis of the effect of upwash on Heat Transfer Coefficients (HTC) and found that under certain setups where the fountain is stable, the HTC is approximately the same in the fountain region as in the impingement region, further increasing heat transfer. Since fountains only occur in unconfined

impingement jets, heat transfer can potentially be significantly improved where such a configuration is possible. Decreasing HTC's and disruptive flow interactions were noted however where jet velocities were reduced or unequal, leading to interactions between the two flows. This highlights the importance of unimpeded flow out of all nozzles in impingement arrays. A diagram is provided in Figure 1.4, as well as CFD results highlighting the velocity contour in Figure 1.5.

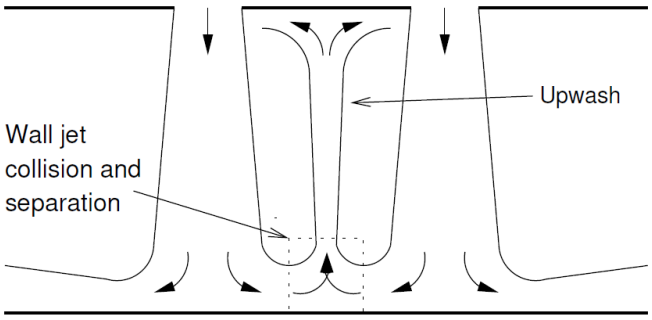

Figure 1.4 – Interaction between 2 adjacent impingement jets leading to upwash [13]

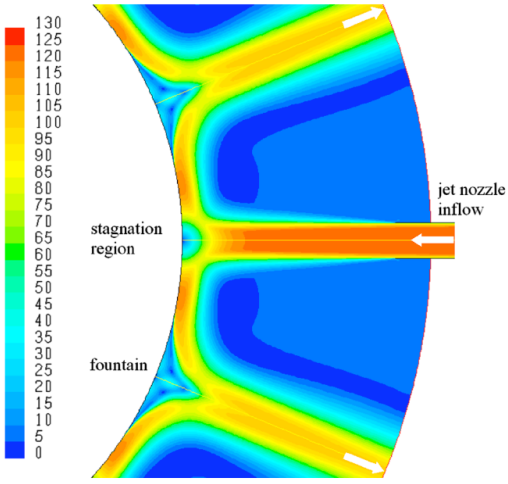

Figure 1.5 – Velocity contours for 2 impinging jets and the resultant upwash, in m/s [14]

The interaction between a jet exiting an orifice and the flow across that orifice is referred to as crossflow. Crossflow can affect heat transfer by reducing overall HTC and causing disruptions to the local HTC [15-17]. Obot and Trabold [15] studied 3 separate crossflow schemes corresponding to minimum,

intermediate and complete configurations. They found that the scheme with the lowest crossflow was best for heat transfer. Xing et al. [16] also found a degradation of cooling performance with higher crossflow schemes. Their maximum crossflow scheme consisted of one outlet, medium consisted of two while the minimum was open on four sides.

Impinging jets can be further classified relative to the fluid of the jet and the fluid the jet impinges through. When the two fluids are the same, the jet is classified as submerged. When the fluid is different, it is classified as unsubmerged. Liquid impinging onto a hot surface in air is an example of an unsubmerged jet impingement cooling application.

This research was initially commissioned to improve the Computational Fluid Dynamics (CFD) modeling of the conjugate heat transfer problem posed by impingement cooling. Accurate and low cost prediction of the wall temperature will improve the design process helping to ensure safety, setting maintenance cycles and estimating the lifetime cost of an engine. For example, blade life may be as much as halved if the wall temperature prediction is inaccurate by a margin of 30°C [2]. Further jet impingement heat transfer may be found in the works of Livingood and Hrycak [9], Hoffman et al. [10], Zuckerman and Lior [8], Li and Garimella [17] as well as work by Gulati et al. [18] on the effect of nozzle geometry on heat transfer characteristics.

Current lifing methods rely heavily on potentially expensive rigs and experimental data to feed into the design process. One such method involves the use of thermochromic crystals on a heated surface which then activate at previously calibrated temperatures. A fixed heat flux is applied to the target plate and the heat transfer coefficient is calculated based on the heat flux necessary to activate the crystals at steady state [19, 20]. Losses to the heater's surroundings can be both minimized and quantified with high confidence. Given that jet impingement creates very high Nusselt numbers in the stagnation region right

under the nozzle exit and relatively low numbers between jets, conduction in the heater itself due to these high gradients can skew results.

The preferred option therefore is heating the jet prior to impingement (e.g. using a mesh heater) and calculating the HTC from this value. This method is seen as more reliable and is the predominant method used in more recent studies [22-25].

1.2 Objective of Current Study

Since experimental methods can require significant financial and time commitments, numerical simulations are being used more widely to reduce cost and streamline the design process. The numerical model's results (i.e. near wall air temperature and HTC) are fed into a Finite Element (FE) model which can then predict the actual metal temperature. Saunders et al [21] describe a process whereby the CFD data is fed into an FE model. In ANSYS, this process can be simply performed by linking boundary layer results from the CFD into a thermal stress analysis tool. The objective of this research is to assess the reliability of the CFD generated data compared to available experimental work. A thorough numerical analysis is performed to ensure a proper numerical setup. Since it was not possible to do an experimental study, the experimental data is extracted from the work of Esposito [22]. Although it may be difficult to replicate the experimental results precisely since certain key inputs such as turbulence intensity are missing, a general assessment of CFD accuracy can nonetheless be made.

Chapter 2. THEORY OF HEAT TRANSFER AND NUMERICAL MODEL

This chapter will outline the underlying principles of heat transfer, jet impingement, fluid motion and turbulence modeling. An overview of the key terms, the Navier-Stokes equations and the defining equations of the turbulence models will be presented, along with any relevant correlations and phenomena.

The key parameter that needs to be validated in the jet impingement heat transfer CFD models is the HTC. HTC can be defined by a simple formula:

$$Heat\ Transfer\ Coefficient = \frac{Specific\ Heat\ Flux}{Temperature\ Difference} \tag{2.1}$$

The formal form of the above equation can be more easily referred to as the Nusselt number. The Nusselt number is key in determining heat transfer. It is a dimensionless number defined as the ratio between convective and conductive heat transfer:

$$Nu = \frac{hL}{k_f} \tag{2.2}$$

where h is the convective HTC, L the characteristic length and k_f the Conductive HTC.

The convective HTC is defined as:

$$h = \frac{-k_f\, \partial T / \partial \vec{n}}{T_{\bar{\infty}} - T_w} \tag{2.3}$$

$\partial T / \partial \vec{n}$ is the wall-normal temperature gradient, $T_{\bar{\infty}}$ is the adiabatic jet temperature and T_w is the wall temperature.

It is known from Newton's cooling law that:

$$q = h(T_w - T_\infty) \tag{2.4}$$

Rearranging the two equations:

$$Nu = \frac{qL}{k(T_w - T_\infty)} \tag{2.5}$$

The Nusselt number can then be found through the flow field results obtained from the CFD solutions. A high Nusselt number would be desirable to maximize heat transfer. The reference (freestream) temperature in this case is taken to be the jet exit temperature while the wall temperature is either given as a constant or derived based on a constant heat flux. The characteristic length *L* is replaced by the jet diameter *D* in this case.

The Nusselt number can often also be defined as a function of the Reynolds and Prandtl numbers through empirical correlations. Some of these may be found in [10, 17] and are of the form of:

$$Nu = a_1 Re^{a_2} Pr^{a_3} f \tag{2.6}$$

where a_1, a_2 and a_3 depend on the flow Reynolds number and f is a function of the geometry.

The Prandtl number is defined as:

$$Pr = \frac{c_p \mu}{k} \tag{2.7}$$

where c_p is the material's specific heat, μ is the dynamic viscosity and *k* is thermal conductivity.

The Reynolds number is defined as:

$$Re = \frac{\rho V L}{\mu} \tag{2.8}$$

where ρ is fluid density, V is flow velocity, L is again the characteristic length and μ is dynamic viscosity.

A further parameter used in the literature is the adiabatic effectiveness [20, 23]. Adiabatic effectiveness is the dimensionless form of the adiabatic wall temperature (the fluid temperature immediately above the wall when the condition of thermal insulation is observed on the surface) and determines the amount of cooling done relative to the total amount of cooling possible [24] . It is defined as:

$$\eta = \frac{T_\infty - T_{aw}}{T_\infty - T_{c,exit}} \tag{2.9}$$

where T_∞ is the ambient temperature, T_{aw} is the adiabatic wall temperature and $T_{c,exit}$ is the coolant temperature at the hole exit.

The adiabatic effectiveness does not take internal cooling or heat conduction into account however and thus is not ideal for impingement cooling. Instead, the nondimensional scaled metal temperature ϕ can be used [25]:

$$\phi = \frac{T_\infty - T_w}{T_\infty - T_{c,internal}} \tag{2.10}$$

where T_∞ is the ambient temperature, T_w is the wall temperature and $T_{c,internal}$ is coolant temperature at the inlet to the impingement holes.

Coolant performance is highest in regions where the heat transfer is lowest (so that the surface is as insulated as possible from the high temperature ambient flow) and where adiabatic cooling effectiveness is as close as possible to 1. These two factors do not necessarily correlate [26].

The Nusselt number of a jet impingement device is highly dependent on the nozzle to distance ratio as well as the flow Reynolds number [2]. Viskanta [27] performed a comprehensive literature review on jet impingement and found that in general, a lower plate distance to nozzle diameter ratio and a higher Reynolds number would increase Nusselt number and the overall heat transfer.

Ichimiya and Hosaka [28] studied both the impact of jet height and the Reynolds number. That lower jet heights and higher Reynolds numbers both result in an increase in Reynolds number. Figure 2.1 shows the values obtained by plotting the Reynolds number against Nusselt number. Where each symbol accounts for a different jet height.

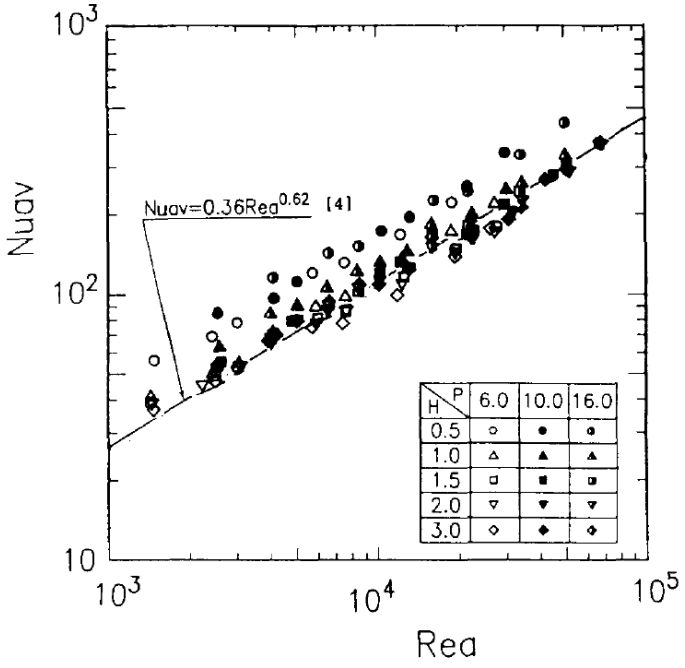

Figure 2.1 – Variation of Nusselt number relative to Reynolds number [28]

Lytle and Webb [29] showed the impact that only changing the jet height can have at a set Reynolds number. Figure 2.2 shows the results of their work plotting maximum local Nusselt numbers for jet to target spacing of 0.1 and 6. The local Nusselt number can be seen to be up to 4 times higher at a set Reynolds number.

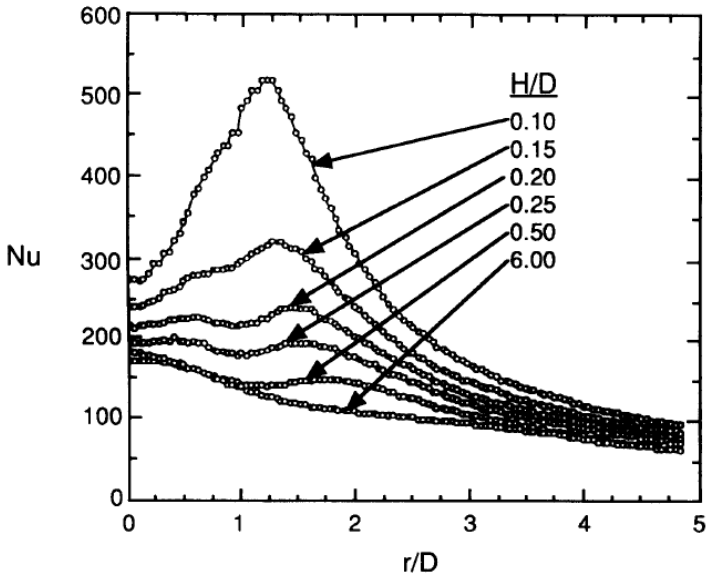

Figure 2.2 – Variation of Nusselt number at different H/D [29]

Their results are supported by the work of Zu and Yan [30] who found a similar pattern as well as Zuckerman and Lior [14]. Zuckerman and Lior [14] performed a numerical study of jet impingement on a cylinder at different Reynolds numbers and jet spacings. They found maximum local Nusselt values up to 16 times higher in the high Reynolds number case than in the low Reynolds number case for the same number of impingement slots and jet spacing at Reynolds numbers ranging from $5x10^3$ to $8x10^4$.

Choo et al [31] also performed a nearly identical numerical study with Reynolds numbers ranging from 500-5,000 and nozzle to plate spacings (*z/D*) of 0.5-10. Confirming the findings of Huang and El-Genk [32] and Gardon [33], O'Donovan and Murray [34] found the presence of a secondary peak in low turbulence jets. Hoogendoorn [35] found two peaks occurring at $r/d \approx 0.45$ and $r/d \approx 2.3$ at low nozzle to plate spacings ($0.2 < x/D < 2$) and low turbulence jets. The high turbulence jet by contrast has a peak at $r/d = 0$ and a secondary peak where the boundary layer transitions to fully turbulent. Figure 2.4 below illustrates the difference in local Nusselt peaks against jet to plate distance.

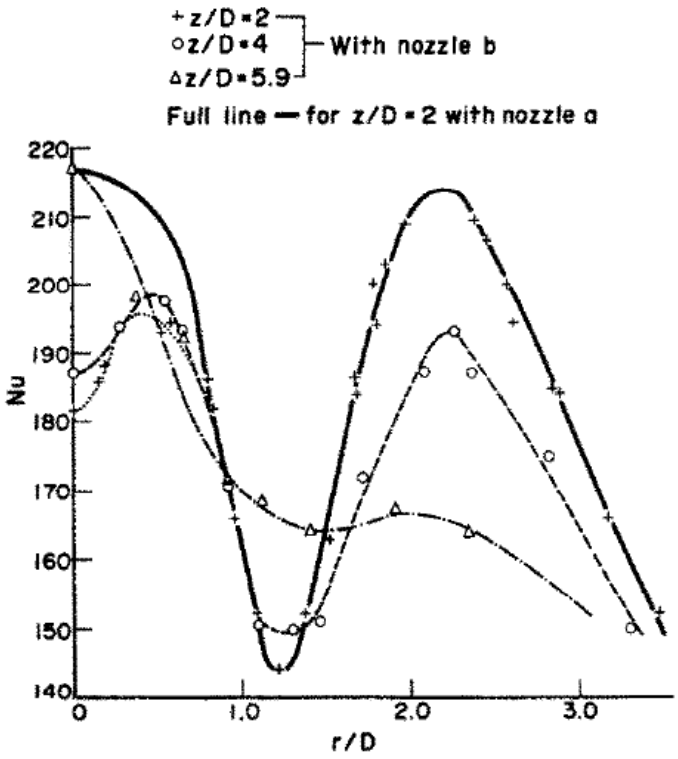

Figure 2.3 – Nusselt Number as a function of r/d at Re= 66,000 - Nozzle "a" is highly turbulent; nozzle "b" discharges a low turbulence jet [35]

The variation of heat transfer seen in Figure 2.3 corresponds to the general form of the Nusselt number at low *z/d* values. Nu undergoes a secondary peak at low nozzle-to-plate spacings which is smoothed out at increasing *z/d* values until it displays only a primary peak.

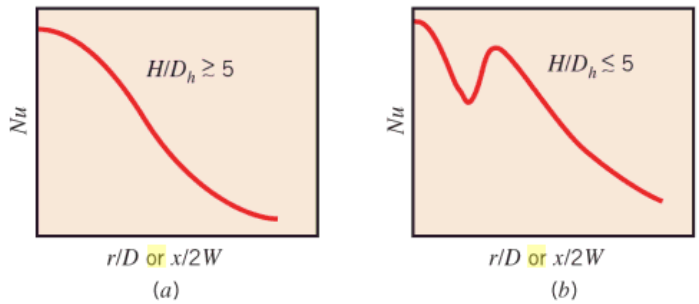

Figure 2.4 – Nusselt number as a function of r/d for a) high nozzle spacings and b) low nozzle spacings [36]

Gardon and Kezios [37] both explain the formation of the first Nusselt number peak by the thinning of the boundary layer to a minimum. The relative Nusselt number minimum following this maximum is explained by the boundary layer being laminar and increasing in thickness until transition to a turbulent boundary layer whereby a second peak is observed. Lytle and Webb [29] attribute the second peak to an increase in the turbulent kinetic energy as distance from the stagnation region increases. Chung and Luo [38] performed a numerical study testing these claims and confirmed the work of Meola et al [39] in that the primary cause of the secondary peak is the generation of vortices from the nozzle exit. The secondary peak of the low turbulence jet begins to disappear as nozzle to plate spacing increases due to interactions between adjacent jets in staggered arrays and interactions with the ambient air [27].

2.1 Mesh Sensitivity

Mesh sensitivity is performed for the purpose of quantifying the difference between the continuous domain and the discretized solution. Mesh independence of the results was verified using the Grid Convergence Index (GCI) of Roache [40], which is based on the Richardson extrapolation. The GCI provides a standardized method of performing grid refinement studies and is a recommended method by the Journal of Fluids Engineering [41]. It should be noted that GCI does not account for faults in problem setup (e.g., bad boundary conditions) or solver shortcomings, but simply provides a standardized method of quantifying discretization errors.

Although GCI can be used with 2 grids using a higher safety factor, it would be impossible to verify that the problem is in the asymptotic region of the solution. It is therefore recommended that 3 grids be used, and so is done in this study. The solution of different grids is compared once convergence of the Root Mean Square (RMS) of the residuals has achieved a certain tolerance (e.g., 3 orders of magnitude) and surface monitors for the desired parameter suggest convergence. Below is the theory behind the GCI method.

Firstly, the grid refinement factor is defined:

$$r = (\frac{N_1}{N_2})^{\frac{1}{D}} \tag{2.11}$$

Where *N* is the number of cells in the grid and *D* is the dimensionality of the problem (2D or 3D). The refinement factor does not have to be an integer, though it is recommended through experience that *r>1.3* [41] (i.e. grid size increases by a minimum of 1.69 and 2.2 for 2D and 3D cases, respectively).

Once the solution has been obtained for the respective grid, the difference in the variable of interest (φ) between the grids is extracted:

$$\varepsilon_{21} = \varphi_2 - \varphi_1 \tag{2.12}$$

$$\varepsilon_{32} = \varphi_3 - \varphi_2 \tag{2.13}$$

If:

$1 > \frac{\varepsilon_{21}}{\varepsilon_{32}} > 0$, then the result is monotonically convergent

$\frac{\varepsilon_{21}}{\varepsilon_{32}} < 0$, then it is oscillatory convergent

$\frac{\varepsilon_{21}}{\varepsilon_{32}} > 0$, then it is divergent.

The apparent order of the method can be calculated using:

$$p = \frac{\left|\ln\left(\left|\frac{\varepsilon_{21}}{\varepsilon_{32}}\right|\right)\right|}{\ln(r)} \tag{2.14}$$

The absolute values must be used in the nominator to ensure extrapolation towards the continuum solution. It should be noted that this equation is only valid for constant grid refinement ratios, as used throughout this work. Extra terms must be introduced in the case of non-constant refinement. Once the order is obtained, the exact solution can be found:

$$\varphi_{exact} = \frac{(r^p \cdot \varphi_1 - \varphi_2)}{r^p - 1} \tag{2.15}$$

The value φ_1 is the solution on the finest grid. The results of the mesh sensitivity done for each case are presented in the respective section. The GCI at each point is also used to calculate error bars to be shown graphically for the variable of interest throughout the domain.

It is also essential to verify that the results are in the asymptotic range. Where 3 meshes are used, a value near 1 suggests asymptotic convergence:

$$\frac{GCI_{32}}{GCI_{21}r^p} \approx 1 \tag{2.16}$$

This will be called the asymptote check value in the following sections.

2.2 Different Turbulence Modelling Procedures

The introduction of turbulence introduces unknowns into the Navier Stokes equations which exceed the number of available equations. To determine the unknowns, a turbulence model makes use of additional equations to resolve the turbulent flow. A turbulent model simulates the effects of turbulence on the

mean flow behavior without resolving all the details of the turbulent behavior. Rather, a turbulent model only resolves details which affect the mean flow. Turbulence modeling is an essential component of modern fluid simulations as many practical applications have Reynolds numbers that fall within the turbulent region.

The general Navier-Stokes equation can be written as:

$$\frac{\partial \mathrm{u}}{\partial \mathrm{t}} + u\frac{\partial \mathrm{u}}{\partial \mathrm{k}} = \frac{1}{\rho}(-\frac{\partial \mathrm{p}}{\partial \mathrm{x}} + \frac{\partial}{\partial \mathrm{x}}\left(\mu\frac{\partial \mathrm{u}}{\partial \mathrm{x}}\right)) \tag{2.17}$$

The approaches to solving the flow equations for a turbulent flow field can be roughly divided into two classes. Direct numerical simulations (DNS) numerically integrate the Navier Stokes equations, resolving all of the space and time fluctuations, without resorting to modeling. In essence, the solution procedure is the same as for laminar flow, except that all the fluctuations in time as well as all eddies must be resolved. As a result, DNS is not practical except for very simple applications. The alternative to DNS found in most CFD packages (including FLUENT) is to solve the Reynolds Averaged Navier Stokes (RANS) equations. RANS equations govern the mean velocity and pressure. They do so by only resolving the time averaged components of the flow that affect the mean flow parameters, splitting the flow into its average and fluctuating component.

The further unknown terms introduced by use of this procedure are resolved by addition of extra equations (i.e. turbulence models). Since the flow is modeled rather than resolved, it must be kept in mind that significant errors may arise from use of models. The addition of a mean and fluctuating velocity component into the Navier Stokes equation yields the time-averaged Navier-Stokes equation:

$$\frac{\partial \rho \mathrm{U}_i}{\partial \mathrm{t}} + \left(\rho U_i U_j\right)_j = -P_i + (\mu\left[U_{i,j} + U_{j,i}\right] - \rho\overline{u_i u_j})_j \tag{2.18}$$

The $u_i u_j$ term, known as the Reynolds Stress Tensor, introduces the unknowns in the equation that require resolution by a turbulence model. The stress tensor describes the transfer of momentum by molecular diffusion and allows for the exchange of momentum between the turbulence and the mean flow.

Since much of the work to be carried out will take place at high Reynolds numbers and with significant stagnation regions, a suitable turbulence model will be required. Work done by previous researchers has shown that the standard k-ε model is inadequate for calculating the wall HTC [42, 59, 60]. This is due to the fact that the k-ε model was developed for pipe wall-parallel flows. The model cannot accurately predict Nusselt numbers near the stagnation region and thus gives HTCs with significant error. The preferred model is V2F due to its accuracy and relatively low computational resource requirements [42, 8] but Shear Stress Transport (SST) models have also been shown to perform to good accuracy in gas turbine heat transfer and jet impingement applications [43, 8, 30]. SST is a RANS model that combines the efficiency of the k-ε model far from the wall and the accuracy of the k-ω model to resolve the low-Re viscous sublayer near the wall. The model was initially proposed by Menter in 1993 [44]. It uses a blending function with a value of 1 in the near wall region and value of 0 in the freestream region to switch between the k-ε and k-ω models. Zu and Yan [30] used the stagnation point of a jet impingement application as test case to compare different turbulence models and found that amongst standard, RNG and realizable k-ε, standard and SST k-ω as well as Reynolds Stress Model, the SST model was the most accurate. The review of turbulence models by Zuckerman et al. [8] for jet impingement applications also found that SST strikes a reasonable compromise between computational resource requirements and accuracy. On the other hand however, Zuckerman [14] found the performance of the realizable k-ε model to be significantly more accurate than the SST model when the flow impinges onto a cylinder. Validation against experimental data will be a necessary step when assessing the accuracy of numerical results. An advantage of SST is its ability to solve either in low-Re mode or as a wall function depending on near wall grid resolution. The wall function method is a collection of semi-empirical formulas which are applied in

the viscous near-wall region and thus remove the need to resolve the flow all the way to the wall. Wall functions have two distinct advantages: Firstly that the turbulence model does not require modification to resolve the near wall flow and secondly that the mesh cell count can be significantly lowered due to placing of the first node at a further distance from the wall. The equations for turbulent kinetic energy *k* and turbulence frequency *ω* in the SST model are given in equations 2.19 and 2.20 below [45]:

$$\frac{\partial \rho \mathrm{k}}{\partial \mathrm{t}} + \frac{\partial \rho \mathrm{U}_j k}{\partial \mathrm{x}_j} = P_k - \beta^* \rho \omega k + \frac{\partial}{\partial \mathrm{x}_j}((\mu + \sigma_k \mu_t)\frac{\partial \mathrm{k}}{\partial \mathrm{x}_j}) \tag{2.19}$$

$$\frac{\partial \rho \omega}{\partial \mathrm{t}} + \frac{\partial \rho \mathrm{U}_j \omega}{\partial \mathrm{x}_j} = \frac{\alpha}{v_t} P_k - \beta \rho \omega^2 + \frac{\partial}{\partial \mathrm{x}_j}\left((\mu + \sigma_\omega \mu_t)\frac{\partial \omega}{\partial \mathrm{x}_j}\right) + (1 - F_1) 2\rho\sigma_{\omega 2} \frac{1}{\omega}\frac{\partial \mathrm{k}}{\partial \mathrm{x}_j}\frac{\partial \omega}{\partial \mathrm{x}_j} \tag{2.20}$$

The terms are defined as:

$$P_k = -(u_i' u_j')\frac{\partial \mathrm{u}_i}{\partial \mathrm{x}_j} \tag{2.21}$$

$$\tilde{P}_k = \min(P_k, \beta^* \rho \omega k) \tag{2.22}$$

$$v_t = \frac{a_1 k}{\max(a_1 \omega, SF_2)} \tag{2.23}$$

$$F_1 = \tanh\left(\min(\max\left(\frac{\sqrt{k}}{\beta^* \omega y}, \frac{500v}{y^2 \omega}\right), \frac{4\rho\sigma_{\omega 2} k}{CD_{k\omega} y^2}\right)^4 \tag{2.24}$$

$$F_2 = \tanh\left[(\max\left(2\frac{\sqrt{k}}{\beta^* \omega y}; \frac{500v}{y^2 \omega}\right))^2\right] \tag{2.25}$$

$$\mu^t = \min(\frac{\rho k}{\omega}; \frac{a_1 \rho k}{SF_2}) \tag{2.26}$$

$$S = \sqrt{2S_{ij}S_{ij}} \tag{2.27}$$

$$CD_{kw} = \max(2\rho\sigma_{\omega 2}\frac{1}{\omega}\frac{\partial k}{\partial x_i}\frac{\partial \omega}{\partial x_i}, 10^{-10}) \tag{2.28}$$

P_k is the rate of production of turbulent kinetic energy, μ_t is eddy viscosity, v_t is kinematic eddy viscosity, *β* and *σ* are constants, *ω* is the turbulence frequency, *S* is the invariant measure of the strain rate, *ρ* is the density, *y* is the distance to the nearest wall, *F1* and *F2* are blending functions which equal to 0 away from the wall and 1 near it to allow the model to switch to the *k-ε* model away from the wall and back to *k-ω* in the boundary layer. Further details can be found in the ANSYS FLUENT manual [46] or Menter [45].

The aforementioned models all solve for steady state problems. In order to model unsteady phenomena, the use of another model, the Large Eddy Simulation (LES) is necessary. LES is a further transient turbulence model that falls midway between RANS and Direct Numerical Simulation (DNS). An LES solution resolves all eddies explicitly but only models eddies smaller than the mesh. This allows it to reduce computational expense relative to DNS, but is still computationally intensive relative to RANS. Its main advantage to RANS models is its improved accuracy while its main disadvantage is the large computational requirement. Due to limited resources, this research is based on steady state results.

2.3 Boundary Layer Resolution

Boundary layer resolution is a key part of resolving turbulent flow problems. Incorrect resolution of the boundary layer can significantly affect the accuracy of key parameters dependent on mass, heat and momentum transfer spanning from the near wall region to the core flow.

The boundary layer can be divided into 3 layers, the viscous sublayer, the buffer layer and the fully turbulent or log-law region.

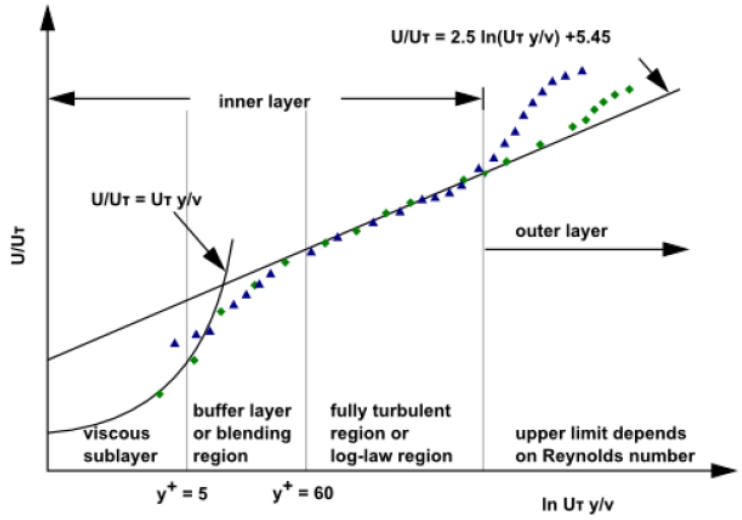

Figure 2.5 – A schematic of different boundary layer sublayers [46]

The boundary layer can be resolved either all the way to the wall (i.e. y+≈1) or using wall functions (i.e. y+>30 or y+>1). Y+ is the nondimensional wall distance and is defined according to equation 2.29:

$$y^+ = \frac{u_* y}{\nu} \tag{2.29}$$

where the friction velocity u_* is$\left(\sqrt{\frac{\tau_w}{\rho}}\right)$, τ_w is the wall shear stress, y is the distance to the nearest wall and ν is the kinematic viscosity of the fluid.

It is recommended that the boundary layer be resolved all the way to the wall for low Reynolds number applications due to the boundary layer potentially not being fully resolved with a wall function approach. The boundary layer is therefore resolved with a first cell y+ value less than 1 on the target plate in all calculations.

Chapter 3. VALIDATION OF TURBULENCE MODELS

Before the geometry of interest was put through the solver, a simple validation study was performed to familiarize with the methodology and assess the available turbulence models. Zuckerman [8] presents an overview of the jet impingement literature and reviews different turbulence models with respect to their accuracy. Naturally, the transient LES/DNS methods are the most accurate, the standard 2 equation models the least accurate, and the V2F model the best compromise between computational cost and accuracy. The V2F model needs to be licensed separately, however, and so was not used in this study. Having obtained an overview of the accuracy of the turbulence models, an analysis was done on the specific case of 2D axisymmetric jet impingement based on the work of Zuckerman [14]. The most suitable model was then selected for the 3D case. The dimensions and boundary conditions are given in Figure 3.1.

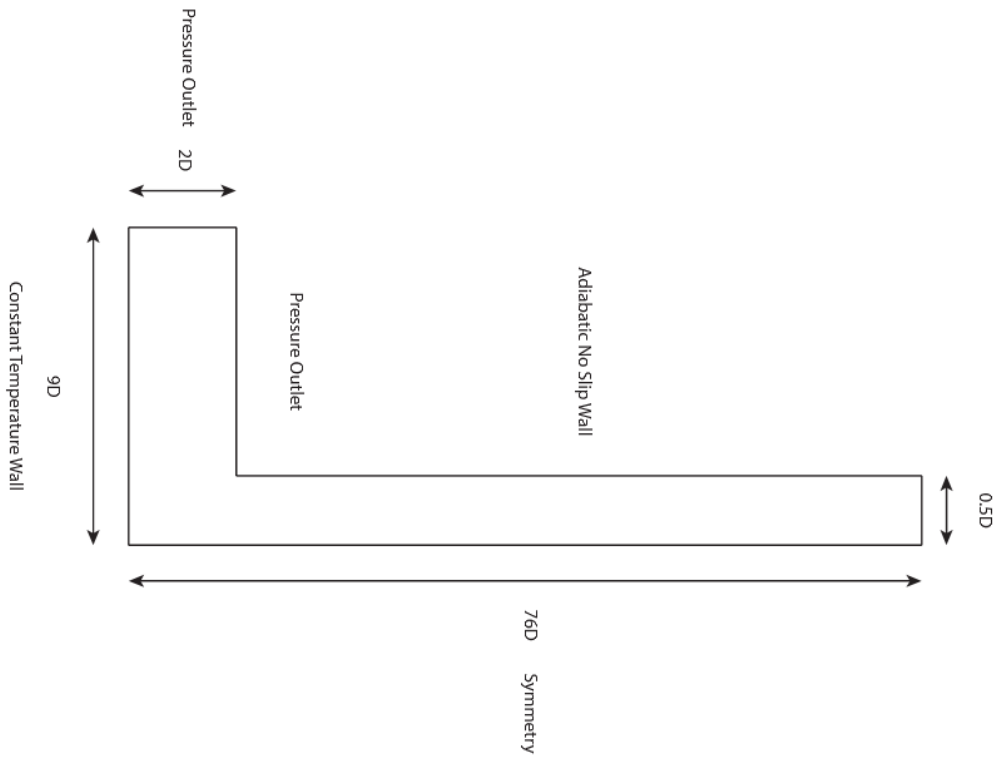

Figure 3.1 – A schematic of the 2D axisymmetric validation case

The diameter was taken as either 1 cm or 3 cm in all cases. The Reynolds number was maintained at 23,500 based on the diameter of the inlet. The jet was modeled as constant density, constant temperature at ambient conditions (300 K) impinging on the target wall of a fixed temperature. The pressure outlets were set to ambient conditions. The heat flux resulting from the constant temperature was then used to determine the Nusselt number. A summary of the boundary conditions is given in Table 1 below:

Table 1 – Boundary conditions for the 2D axisymmetric case

Domain Boundary	**FLUENT Condition**	
Inlet	Velocity Inlet	Reynolds=23,500
Outlet	Pressure outlet	0 Gauge Pressure
Impingement surface	Wall	Constant temperature of 315K for ΔT of 15K
Axis	Axis	-
Pipe Wall	Wall	No-slip wall

The solutions were derived using both first order and second order upwind schemes. First order schemes were used for comparison to Zuckerman [14] while the more accurate second order scheme was used to select the turbulence model.

The SIMPLE scheme with default underrelaxation values were used throughout for the sake of numerical stability and timely convergence. The results were deemed to be converged once the residuals had reached 10^{-4} or 10^{-5} and more importantly, no more significant changes occurred in the Nusselt number based surface monitor on the target surface. A sample mesh can be seen in Figure 3.2.

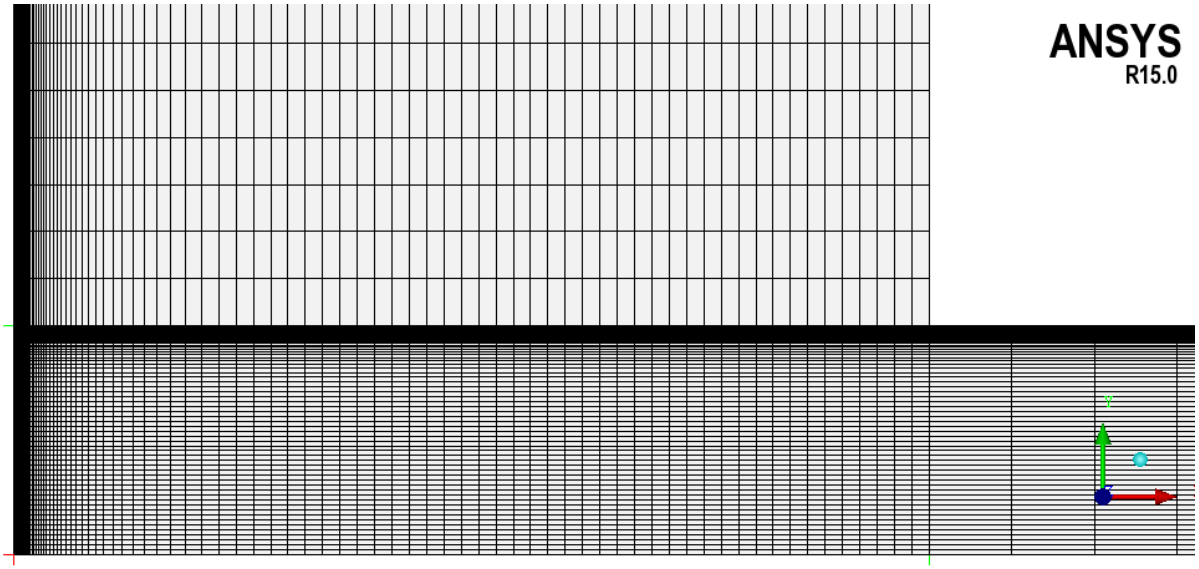

Figure 3.2 – Sample of the mesh used for the 2D axisymmetric validation case

The flow enters from the right in the above image and impinges on the surface at the left (where the mesh becomes finer). The pipe is sufficiently large (>60 *D*) for the flow to be fully developed as it exits the pipe. The max *y+* values in the entire domain are kept <1.5 in all cases in order to resolve the near wall viscous region as part of the solution.

Ideally, volume change in the mesh between adjacent cells is kept to a minimum (e.g. 20%), though in the mesh used above there is significant change between the free jet region and the stagnation region. This can result in erroneous results but since all the models were verified on the same mesh, the effect in this case is assumed to be minimal.

The resulting Nusselt number values of each turbulence model are given in Figure 3.3 and Figure 3.4 below. Results are based on a mesh size of 40-60k cells (coarse mesh results are omitted to avoid cluttering).

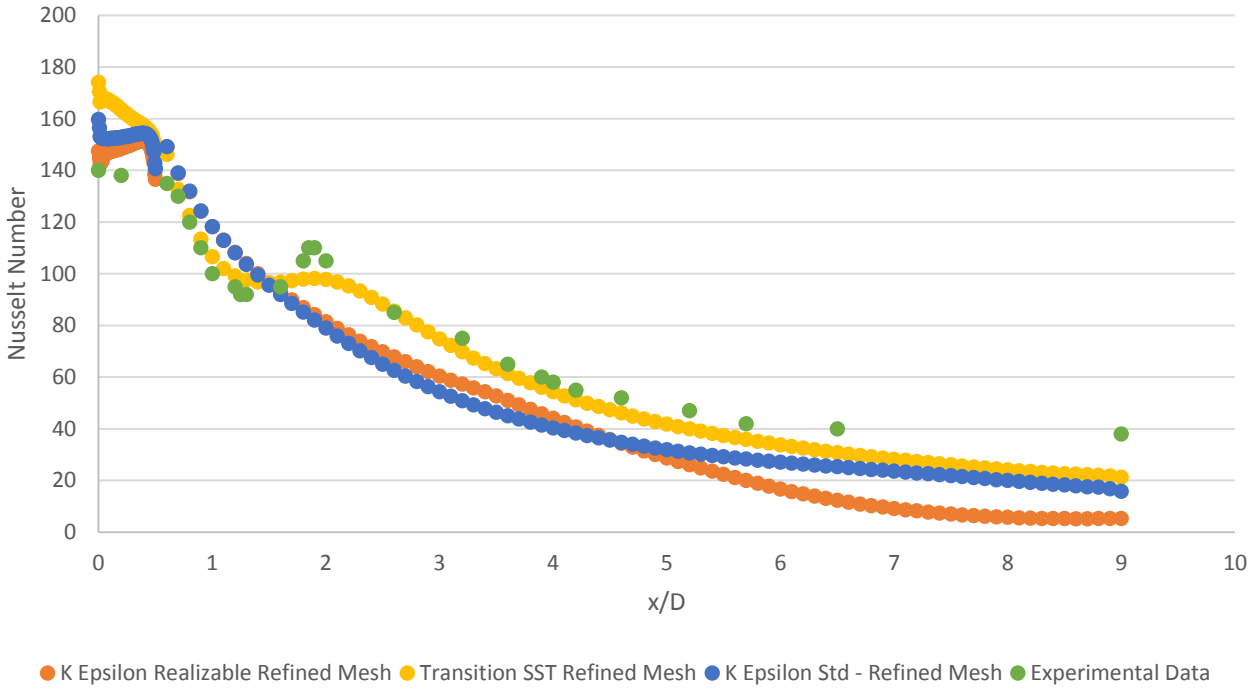

Figure 3.3 – Nusselt number distribution for the 2D axisymmetric validation case using different k-ε turbulence models (refer to [47] for experimental results)

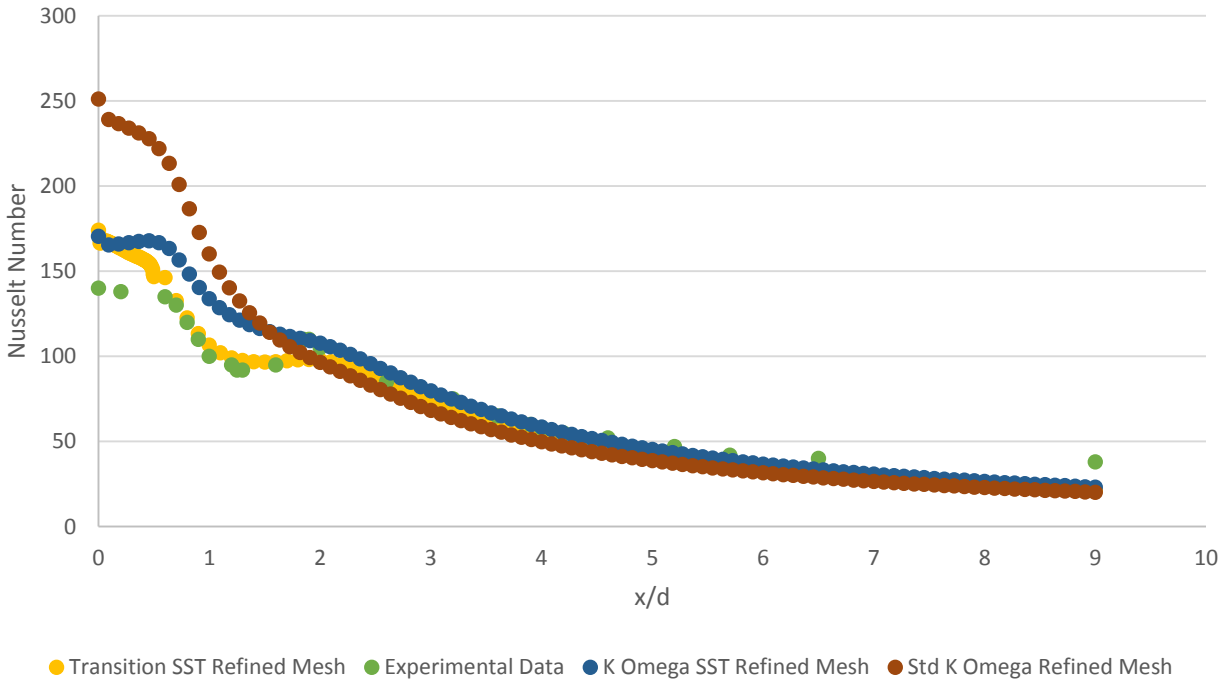

Figure 3.4 – Nusselt number distribution for the 2D axisymmetric validation case using different k-ε turbulence models (refer to [47] for experimental results)

The first set of results compares the *k-ε* model to the experimental and Transition SST model, while the second set compares the *k-ω* models.

The 4 equation transition SST model follows the experimental results with the highest overall accuracy, but at the expense of a higher computational time due to the 2 added equations relative to the *k-ω* and *k-ε* turbulence models. The standard *k-ω* model vastly overestimates the Nusselt number in the stagnation region, but performs well in the wall jet area. *K-ω* SST is the only 2 equation model that shows the second peak referred to by previous researchers and in the experimental results of Baughn [47]. Although it overpredicts the stagnation region average nusselt number by approximately 20% compared to the *k-ε* models' 10%, it is the most accurate model over the full stagnation and wall jet regions. A linear regression analysis done on the two cases with respect to the experimental results over the full surface shows that the *k-ω* SST model fits the data with an R^2 value of 97.01% while the *k-ε* realizable model has a fit of 94.78%. The standard error for the *k-ω* SST model stands at 5.850 and 7.644 for the *k-ε* realizable model.

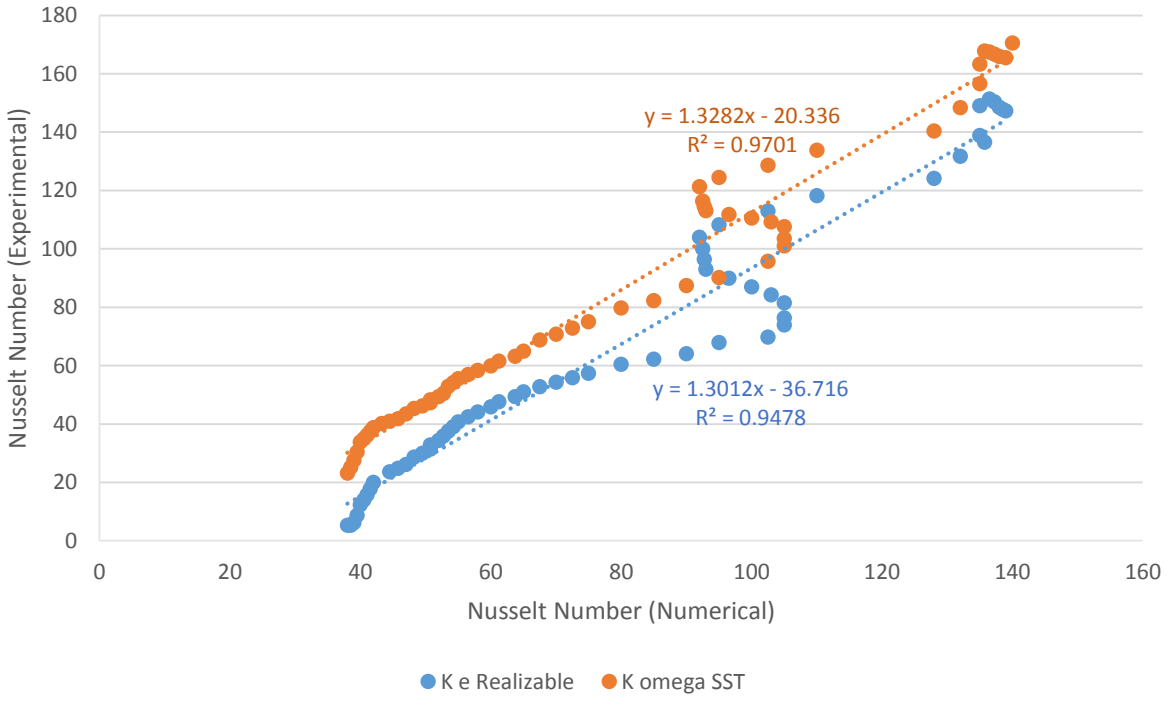

Figure 3.5 – Linear regression analysis for k-ε realizable model against k-ω SST model based on the 2D axisymmetric case

So though both models can be effective, the *k-ω* model is somewhat more accurate. It is therefore the chosen model as it provides the best compromise between computational efficiency and accuracy. It will be used on all the following 3D cases.

Having chosen the model, a mesh sensitivity analysis was performed. The results are shown in Figure 3.6 below.

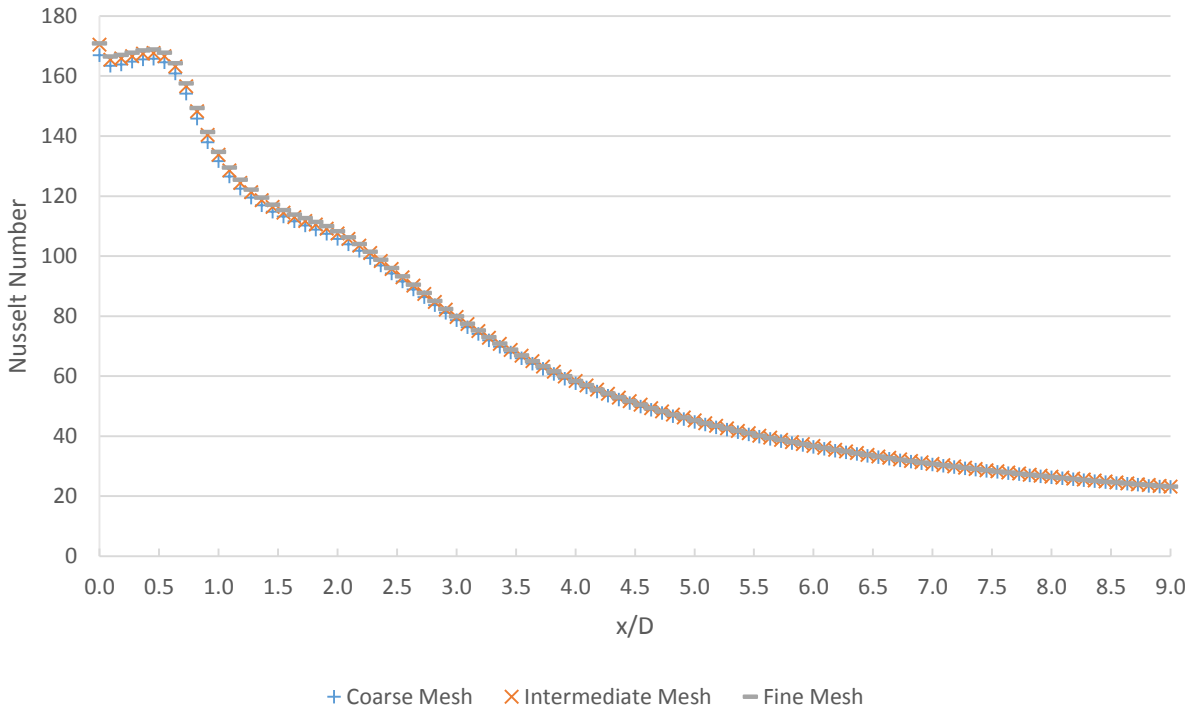

Figure 3.6 – Mesh sensitivity analysis for the 2D axisymmetric validation case

The stagnation region is the area where mesh refinement is most effective due to the complexity of the flow. The three meshes have the greatest difference in the stagnation region but refinement does not significantly increase accuracy in the wall jet region. An error bar graph is not displayed due to the local GCI values all being <0.5% on the fine grid solution (and therefore difficult to see graphically). The refinement ratio was 2, resulting in a 4 times increase in the cell count for each grid due to the 2 dimensional domain.

The Nusselt numbers on each mesh were averaged over the full target surface and used to derive the continuum solution in Table 2.

Number of Cells	***Max y+***	***Area Averaged Nusselt Number***	***GCI***
10 x 10^3	1.237	2473.059	
40 x 10^3	0.622	2505.617	10k to 40k 2.32%
160 x 10^3	0.424	2515.081	40k to 160k 0.674%
Non-Discretized Solution		2518.960	

Table 2 – Results of the mesh sensitivity analysis for the 2D axisymmetric case

The non-discretized solution is extrapolated based on the intermediate and fine mesh values. It is based on the assumption of the measured value reaching an asymptote approaching the continuum solution with sufficient grid refinement. In this case, the difference between the non-discretized solution and the intermediate (40k) grid is negligible, and so the grid is assumed to be sufficiently fine. The problem was based on the work of Zuckerman and Lior [8] and Seldov and Ivanov [48], neither of whom performed a mesh sensitivity analysis. They used grid sizes of 44k and 290-390k cells for similar geometry, respectively. This suggest that the 44k mesh size is a better compromise between accuracy and computational resources than the far larger grid of Sedlov and Ivanov [48].

The contours of velocity and turbulent kinetic energy are given in Figure 3.7 and Figure 3.8 for the selected mesh of the κ-ω SST model.

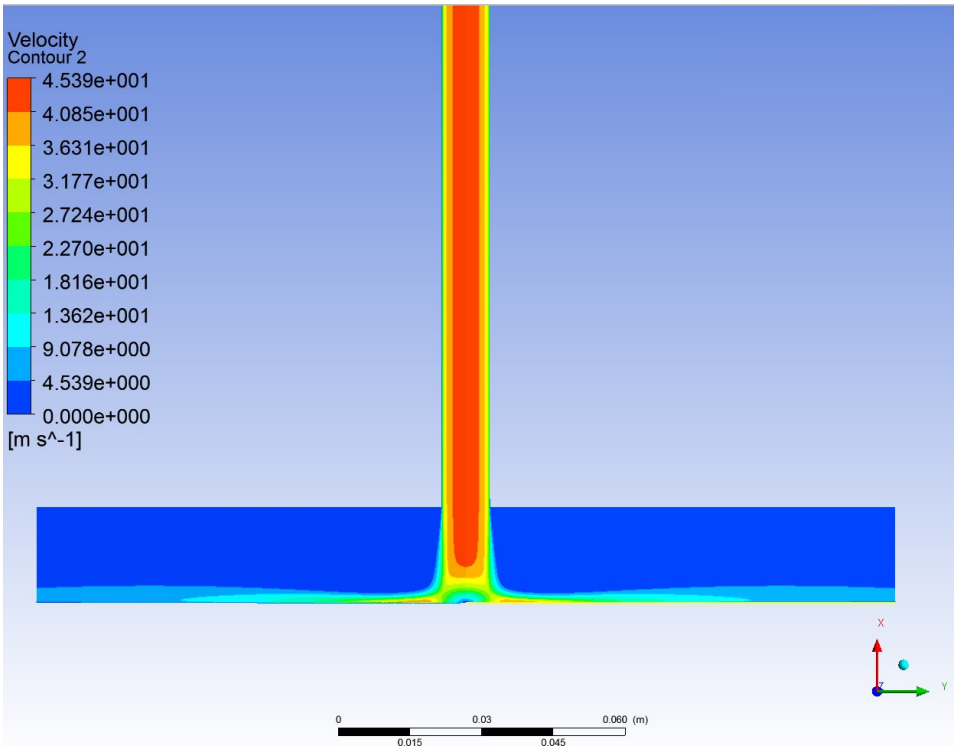

Figure 3.7 – Velocity contours of the 2D axisymmetric case

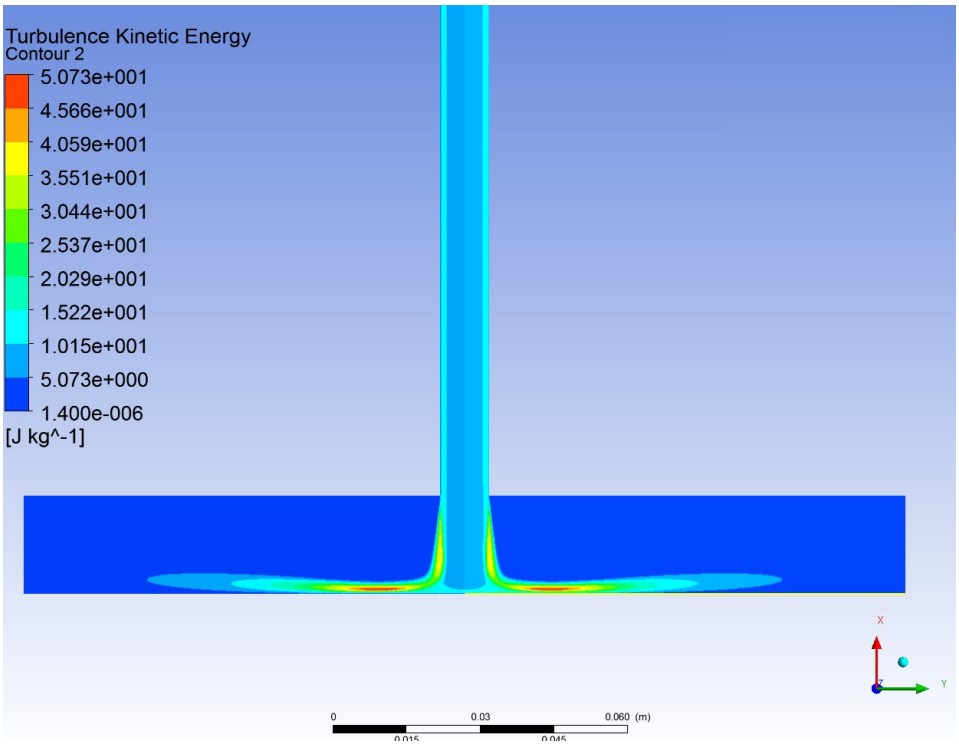

Figure 3.8 – Turbulent kinetic energy of the 2D axisymmetric case

Turbulence increases around the jet during its exit due to entrainment from the surrounding flow and also as the jet accelerates again in the wall jet area. The corollary to the high turbulence energy region is seen in the Nusselt number graph as the secondary peak of the Nusselt number.

Chapter 4. APPLICATION AND ASSESSMENT

The purpose of this study is to further compare the experimental results obtained by previous researchers [22, 16] to determine whether CFD is a reliable replacement for more costly and time consuming experimental studies. The paper that is the focus of this work is that of Esposito [22] and his experimental work in comparing the cooling efficiencies of several different geometries in a jet impingement heat transfer study. It was found in the experimental work that a corrugated geometry can improve heat transfer rates in the stagnation region and overall in the spanwise direction. The two geometries are tested in ANSYS FLUENT to determine whether CFD could reliably predict this behavior and with an acceptable margin of accuracy. For that purpose, the CFD domain replicates the experimental domain.

4.1 GEOMETRY

The first case to be analyzed was the basic flatplate impingement. This is the most basic geometry, consisting only of an impingement plate with inlets, a target surface for the jet to impinge on and an outlet, with the impingement chamber surrounded by walls. Some researchers include a plenum [49-52] while others do not [16, 49, 50] though the case of Singh et al. [49] concerns impingement on a cylindrical surface and imposes a fully developed velocity profile at the domain inlet/pipe exit. The presence or lack thereof of a plenum and influence on results will be discussed later in this chapter. The basic geometry and parameters are shown in Figure 4.1 and Figure 4.2 below.

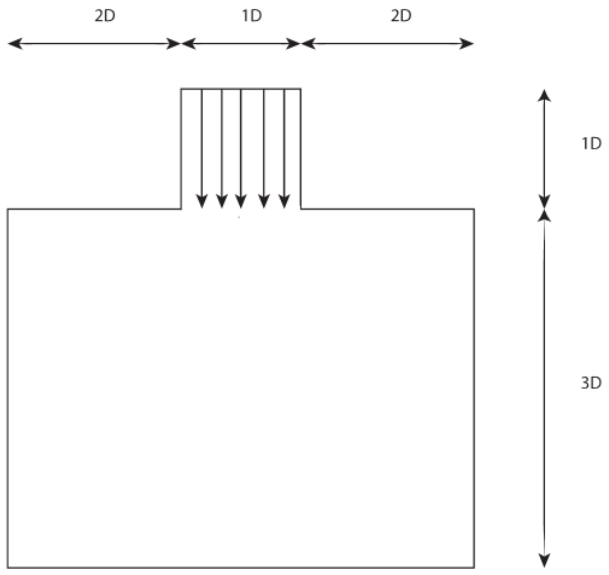

Figure 4.1 – Dimensions and layout of the basic flatplate case

The geometry was drawn up in ANSYS DesignModeler based on the experimental parameters. The geometries were run at an impingement distance (*z/d*) of 3, the results of which are available in the experimental study [22]. The actual inlet diameter used in all cases was 3 cm, resulting in an inlet velocity of 10-30 *m/s* for the available Reynolds numbers (20-60k).

The second case was the corrugated impingement. The width of the geometry is kept the same as the basic impingement case, but with corrugations parallel to the stream direction. The corrugations are meant to direct the crossflow away from the downstream jets and therefore improve cooling effectiveness. This was seen quite clearly in the experimental results, the numerical results will be verified for this trend. The geometry is described in Figure 4.2.

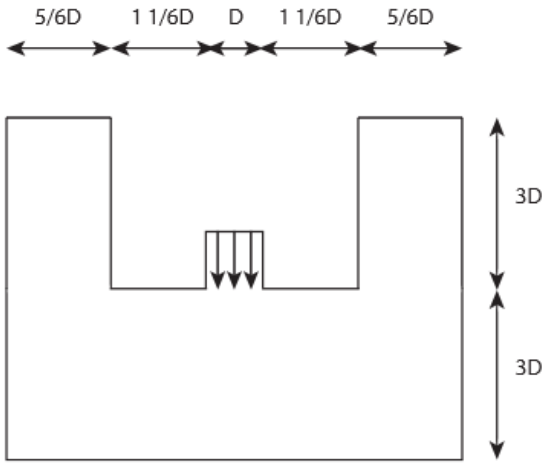

Figure 4.2 – Dimensions and layout of the corrugated case

In both cases, the distance between the center of the inlets both in the streamwise and the spanwise direction was 5 *D* while the outlet was placed a distance of over 30 *D* downstream to eliminate the possibility of interaction with the flow. In the experimental setup, each geometry consisted of 5 rows of 10 holes surrounded by 3 walls and an outlet in the impingement chamber. In order to minimize wall effects on the flow, the two outside rows were disregarded and data was collected only for the 3 middle rows. This configuration allows the CFD domain to be further simplified into 1 row bounded by 2 symmetries on the sides, a no-slip wall on one end and a pressure outlet at ambient conditions on the other. The boundary conditions are listed in Figure 4.3.

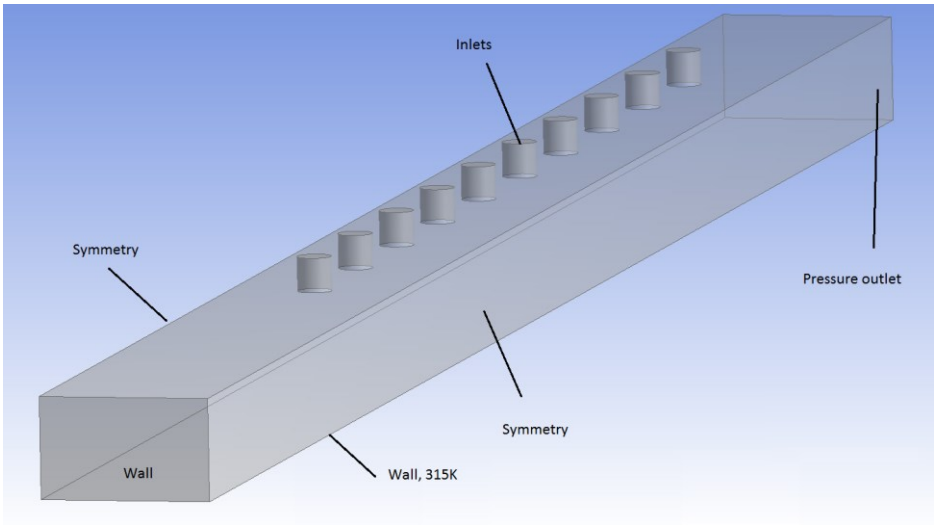

Figure 4.3 – Boundary conditions for each case

4.2 MESH

The geometry files were exported to and meshed in ICEM 14.5. An unstructured hexa mesh was used throughout the domain with O grids placed on the inlets to improve orthogonal quality. O grids are grids where the first cell meets the last cell in a loop. The use of o grids on curved surfaces drastically improves cell quality by allowing for a smooth transition from the curved surface to the inner cells. Using the Determinant 3x3x3 quality metric in ICEM to assess the mesh, minimum values ranged from 0.45 to 0.7. A determinant value of 0 indicates a fully degenerated cube with negative volume, while a value of 1 indicates a perfect cube. A minimum determinant value of >0.3 is generally acceptable for most solvers [51]. A minimum value of 0.45 or 0.7 was obtained, depending on whether wall functions were used at the inlet pipe walls or the domain was resolved all the way through the viscous sublayer (therefore requiring a finer mesh and higher cell count at the wall). Although the mesh quality was lower where the viscous sublayer was fully resolved, the wall function assumption of an extended log layer is not valid

where the Reynolds number is smaller than 10^6, resulting in the near wall approach being used throughout the domain. Two examples of meshes for both the corrugated and the simple flatplate are provided in Figure 4.4 and Figure 4.5.

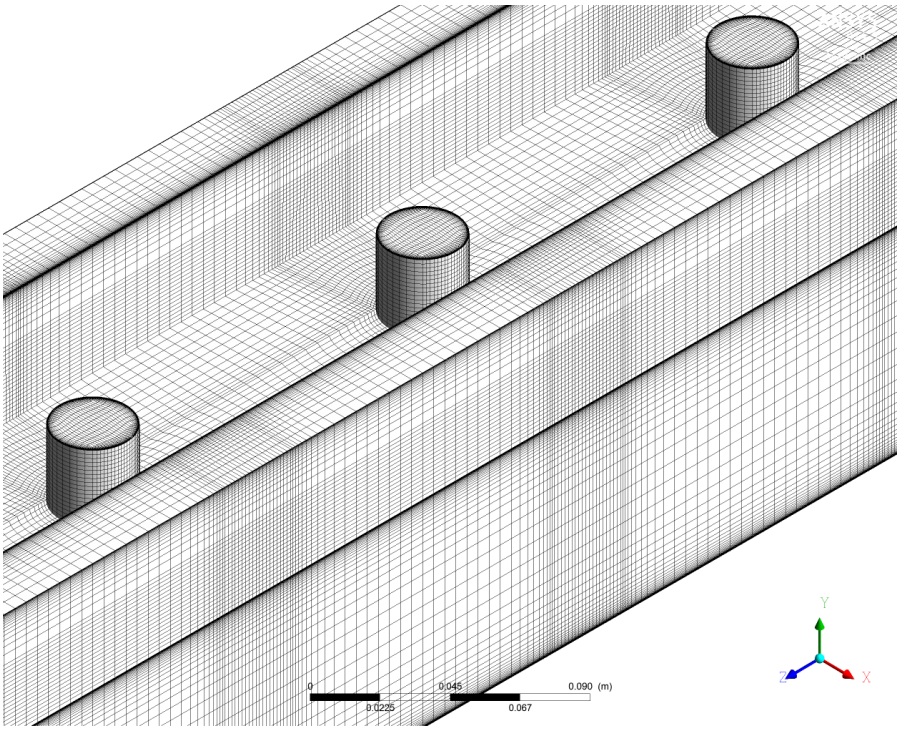

Figure 4.4 – Sample mesh of the corrugated case

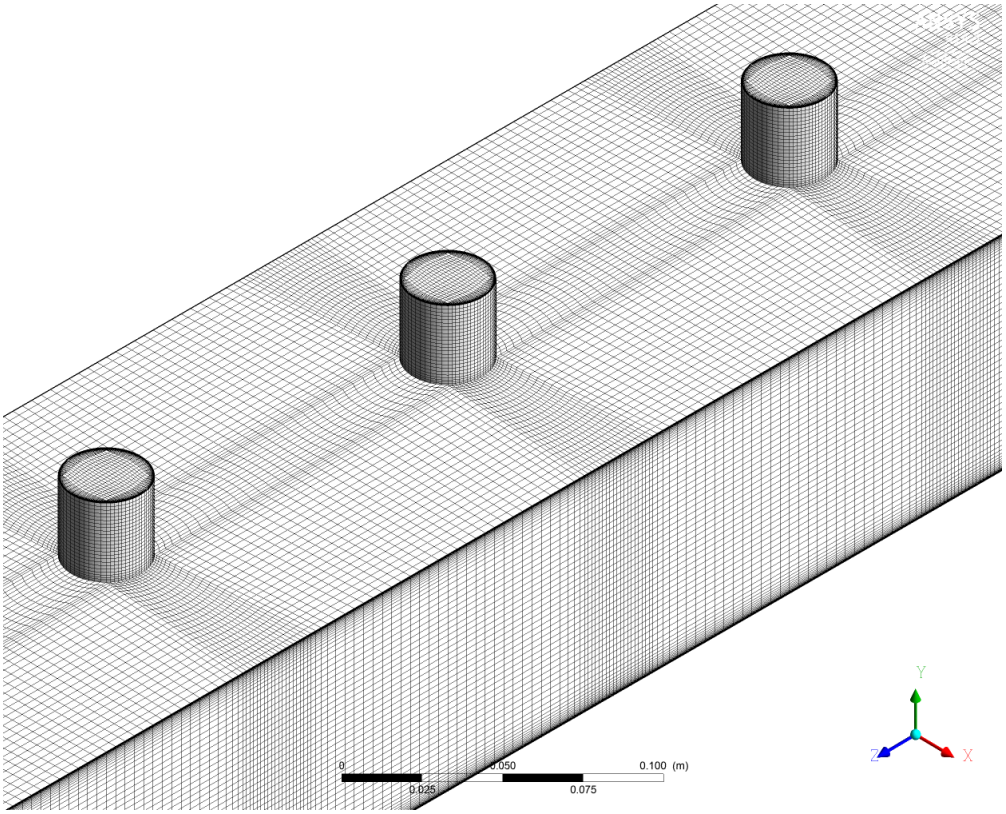

Figure 4.5 – Sample mesh of the basic flatplate case

The mesh was made finer in the near wall region throughout the domain at a constant growth ratio not exceeding 1.2 for both accuracy and numerical stability. The y+ values were kept at <2 on the target plate. Grid refinement, as discussed in Chapter 2, was performed using the GCI method of Roache [40], which uses Richardson extrapolation to obtain a continuum solution. 3 structured meshes were built with a constant refinement factor of 1.3, therefore increasing cell density by 1.3 in each axis. In the 3 dimensional domain, this results in the cell count increasing by a factor of approximately 2.2. All 3 meshes were tested at a Reynolds number of 20,000 and the results were deemed applicable to the other values. The coarse mesh is roughly 2 million cells, the intermediate mesh is approximately 4 million cells while the finest mesh consists of around 9 million cells. The average target surface Nusselt number was calculated on each

mesh and used to determine the order, the GCI, the relative errors and whether the meshes were in the asymptotic range.

Both cases resulted in an asymptote check value of approximately 1, suggesting that the meshes are in the asymptotic range. Both cases are therefore converging, though the corrugated geometry seems to be more accurate than the flatplate mesh. The area averaged Nusselt values are seen in Figure 4.6.

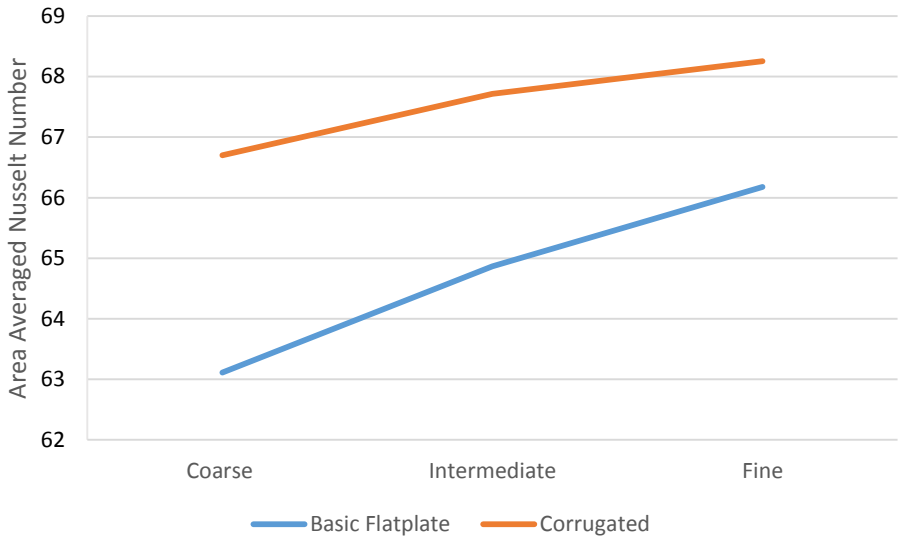

Figure 4.6 – Mesh Sensitivity results of the 3D case for both geometries

The discretization error was seen to be below 10% in both cases, so a medium mesh is used as a better compromise between accuracy and available computational requirements in all runs. The local errors were calculated on the centerline for comparison to previous work and results are shown in Figure 4.7 and Figure 4.8.

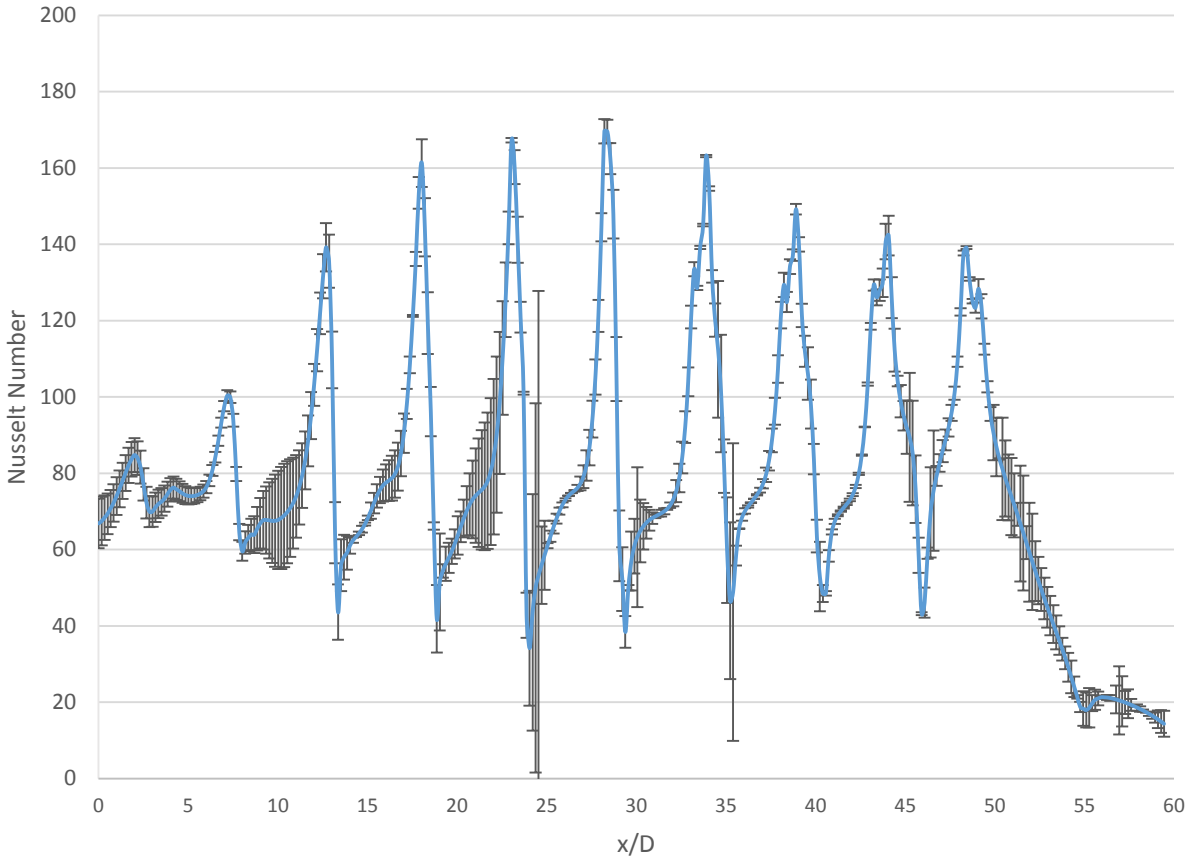

Figure 4.7 – Local discretization errors at the centerline for the basic flatplate case

The centerline is a line on the impingement surface stretching from the wall on one end of the domain to the outlet on the other through the middle of each impingement hole.

The stagnation regions where heat transfer is highest do not have significant discretization errors, so the mesh is deemed sufficiently close to the continuum solution.

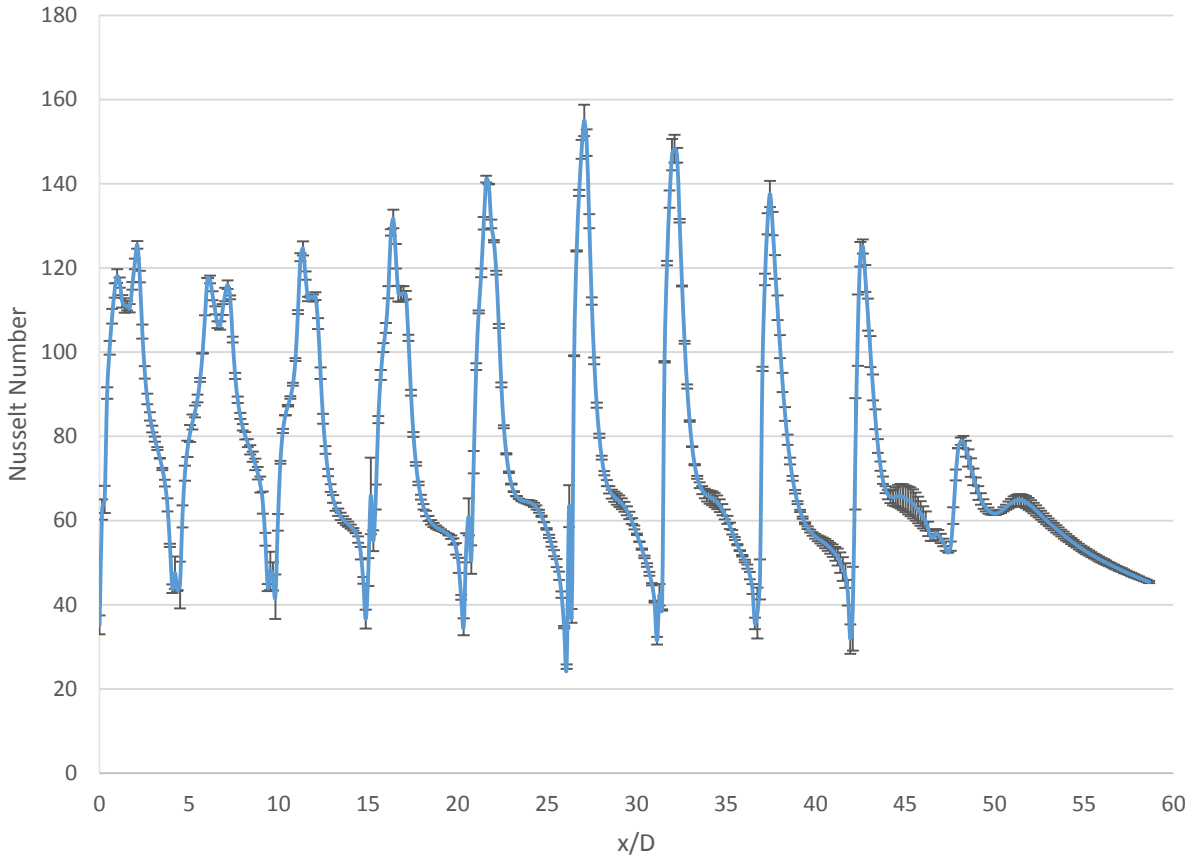

Figure 4.8 – Local discretization errors at the centerline for the corrugated case

The corrugated mesh is closer to the continuum solution than the basic geometry. Local errors appear to peak just after the impingement region (area with the highest Nusselt number) in each jet in the corrugated geometry. The basic flatplate geometry seems to have the highest local errors just behind each jet, while the corrugated geometry seems to have the highest local error right after the stagnation region under each jet. The errors are deemed negligible to the overall solution however, as the highest heat transfer regions are not significantly affected by the discretization errors.

4.3 COMPUTATIONAL SETTINGS

The model was run using ANSYS FLUENT 14.5 on the local computer. The processing unit was an i7-4770 Quad Core with 16GB of RAM and a mechanical hard drive. Since the CPU was serviced by 8 threads, parallel processing with 8 cores was enabled. The mesh was imported via the ANSYS workbench and scaled based on the inlet diameter. The turbulence model used is the *k-ω SST* model with the energy equation enabled. The velocity did not exceed 42 m/s in the domain in the fastest case, therefore $M<0.3$, so compressibility effects could be ignored. The air was modeled as constant density with $\rho=1.225$ kg/m^3. All relevant property values (e.g., viscosity, thermal conductivity) were as standard for air at 300K. There is a total of 10 velocity inlets, which at a scale of 3 cm each have a velocity value of 10-30 m/s depending on the required Reynolds number. The hydraulic diameter method was used to determine the turbulence length scale with a turbulent intensity of 5%. Since turbulence intensity was not measured in the experimental setup, this value is an approximate guess. The outlet was a pressure outlet at ambient conditions, with symmetry on the sides, no slip walls on the impingement plate and a no slip wall at a temperature of 315 K as the target surface. The Nusselt value was calculated based on the heat flux required to maintain the constant temperature of the surface.

The second order upwind scheme was used for momentum, turbulent kinetic energy, specific dissipation rate and energy with a standard method for pressure. Default underrelaxation values were used unless necessary to facilitate convergence, where typically pressure would be set to 0.2, momentum and turbulent kinetic energy and dissipation rate were set to 0.5 as recommended by the FLUENT software developer [46]. A surface monitor for heat flux/Nusselt number was set at the target surface to monitor convergence in addition to the residuals. The lowest Reynolds number case was run first, and initialized using either the inlet conditions or FLUENT's hybrid method which solves for the pressure and velocity fields using Laplace's equation. Once convergence had been reached, typically at 10^{-4} and with negligible

changes in the surface monitor, the data was then written and interpolated onto the following higher Reynolds numbers cases to accelerate convergence.

4.4 Results and Comparison

The 20,000 Reynolds number case was the first case to be conducted. The experimental and the CFD contours are provided for comparison in Figure 4.9-4.11. Each contour shows the distribution of the Nusselt number on the target surface for the set geometry at each Reynolds number.

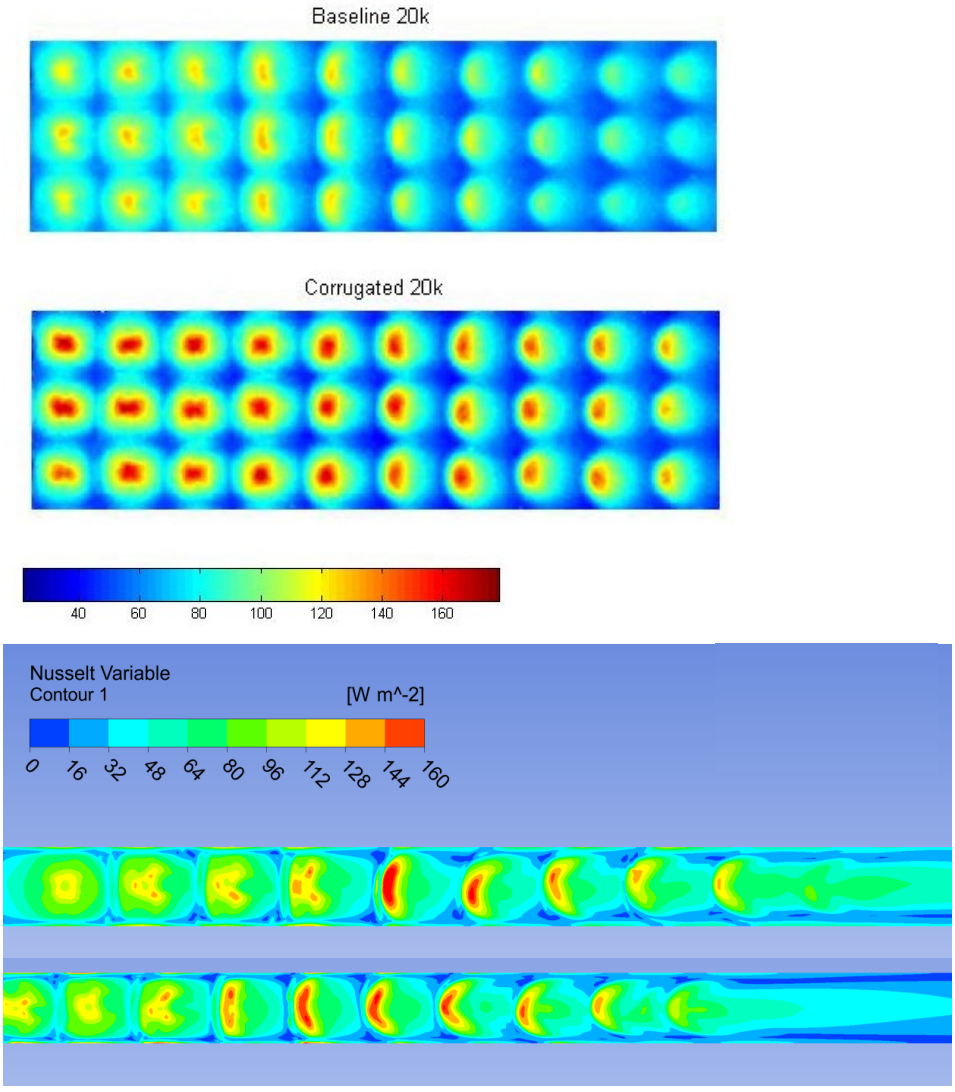

Figure 4.9 – Nusselt contours at Re=20,000 for both the basic flatplate and corrugated geometries; Experimental [22] and CFD

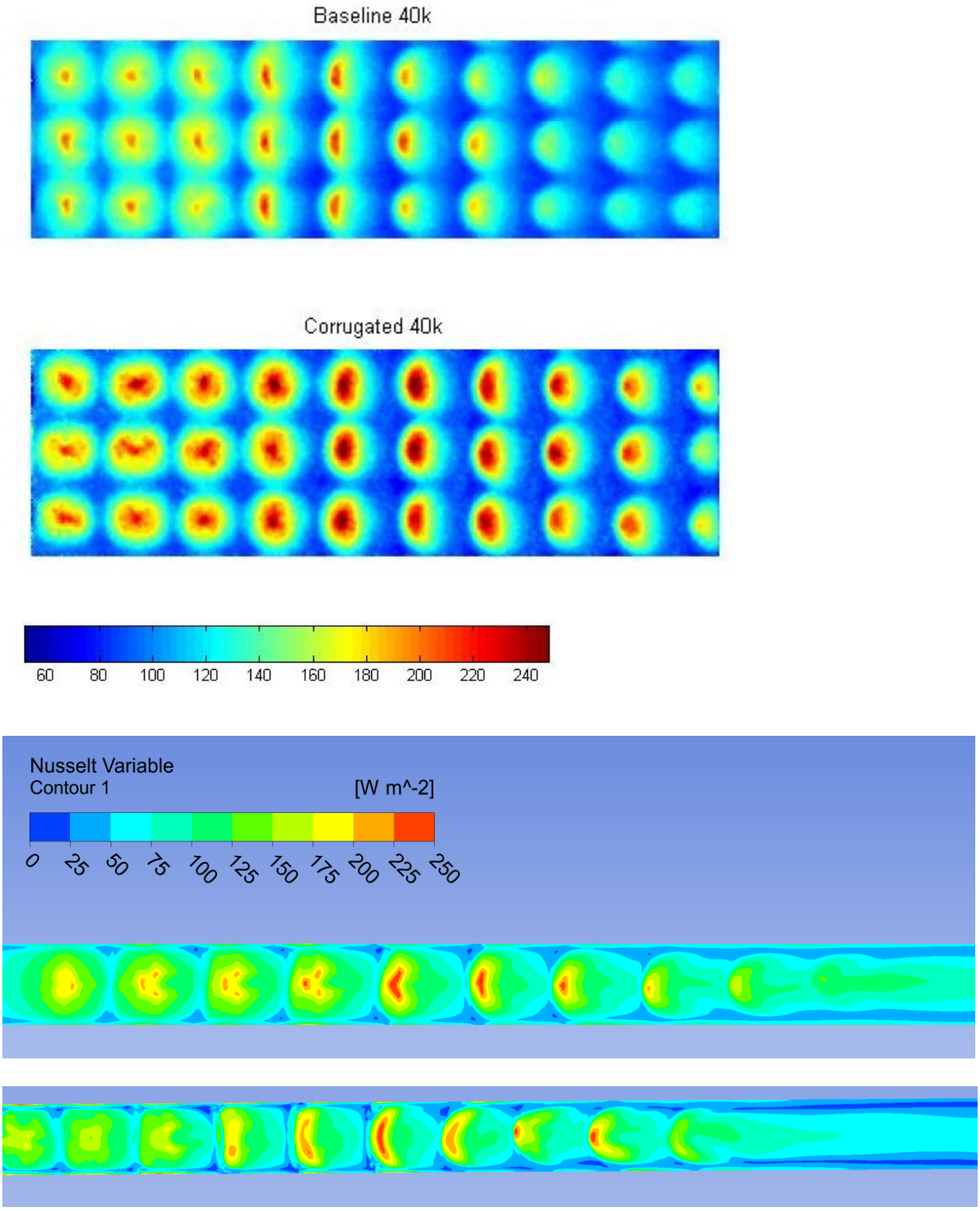

Figure 4.10 – Nusselt contours at Re=40,000 Reynolds for both the basic flatplate and corrugated geometries; Experimental [22] and CFD

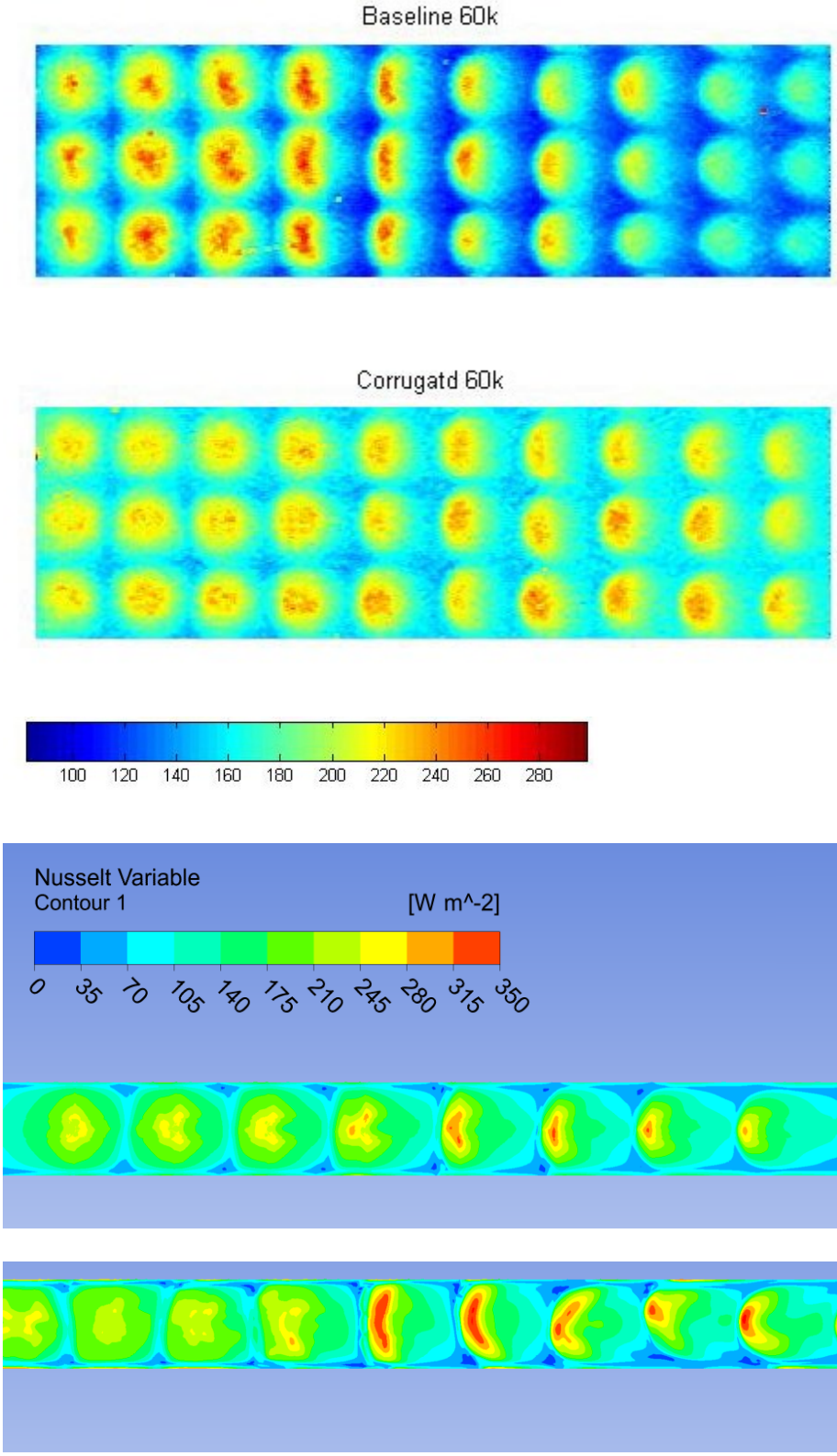

Figure 4.11 – Nusselt contours at Re=60,000for both the basic flatplate and corrugated geometries; Experimental [22] and CFD

All the contours seem to show that the experimental and CFD flow patterns are not replicated exactly, particularly in the stagnation regions. This error may be negligible at lower Reynolds numbers but becomes more significant as the jet velocity increases. This trend of increasing error at higher Reynolds numbers has also been seen in other recent works [52]. Whereas the experimental results show the baseline geometry Nusselt values peaking from the 4th-5th jet, the CFD results show the peak on the 5th-6th jet regardless of the Reynolds number. This increase in Nusselt value may be attributed to the initial effect of the crossflow. As the crossflow to jet velocity is initially low, it only increases the stagnation region and thus the local Nusselt values. Since the flow can only exit through one direction however, the flow accelerates downstream to the point where it begins to degrade the performance of the following jets. The numerical solution does replicate the experimental work of Xing [16] and Rao [50] however, see Figure 4.12.

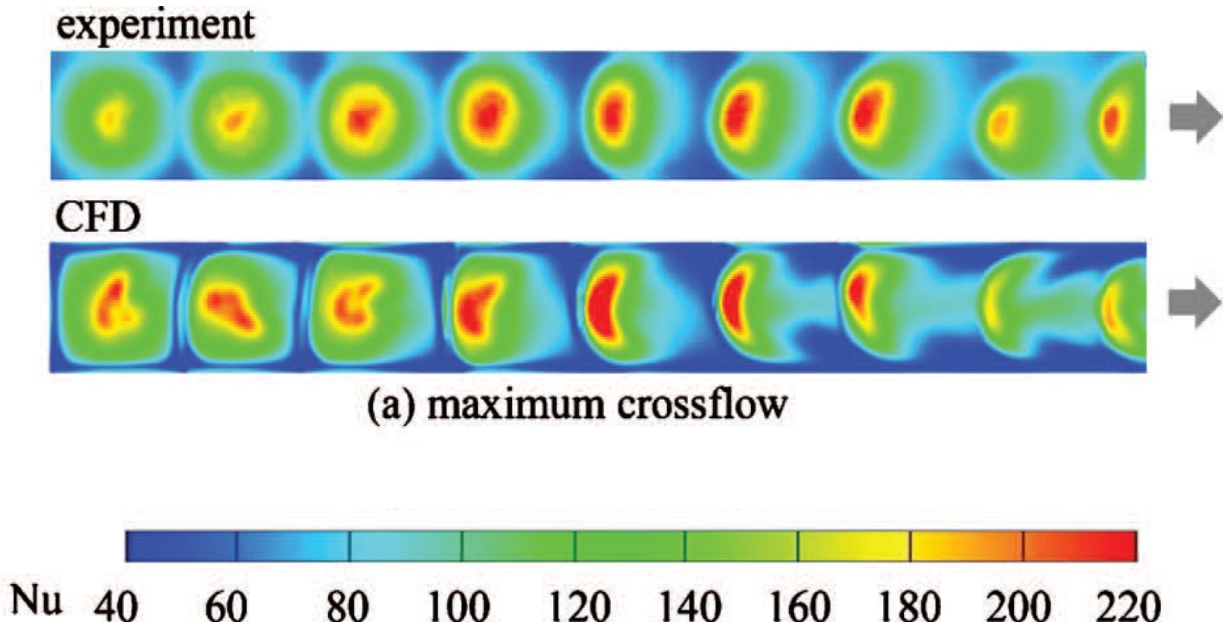

Figure 4.12 – Experimental and CFD results of a basic flatplate case at Re=35,000 [16]

Xing's results used virtually the same geometry as Esposito and as in this study, with *z/d=3* and *x/d* and *y/d=5*, at a slightly lower midrange Reynolds number. Both used a similar experimental setup, though Xing

places the heater mesh before the plenum whereas Esposito places it right above the impingement plate. Neither papers measured turbulence intensity, so it is possible that a difference in the setup could have affected turbulence before entry through the impingement plate and caused the flow profile to change. Both make the assumption of an infinite wall and make measurements over a small enough time period that the assumption would hold valid, though the mesh response for the two is different. Whereas the mesh heater of Xing had a response time of 0.3s, Esposito achieves the step temperature change in 0.03s. This should not however highly impact the results as the heater response delay can be rectified, for example through Duhamel's superposition integral [53]. To quantify the error, the Nusselt number is averaged at short intervals in the spanwise direction along the length of the geometry for each case. Approximately 400 lines were drawn for each case using an automated script in CFD Post (given in Appendix I), with an averaged Nusselt/heat flux variable linked to each line. Each value was then exported and plotted. The results are displayed in Figure 4.13-4.15.

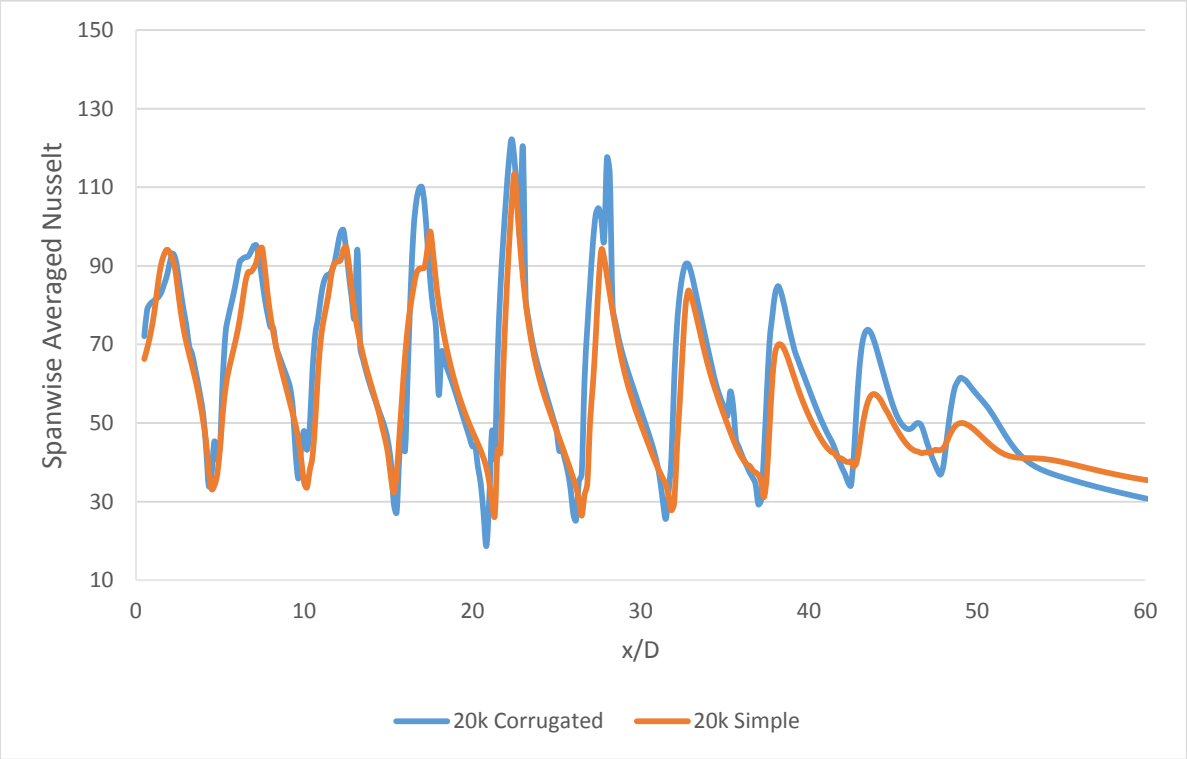

Figure 4.13 – Spanwise averaged Nusselt number for each numerical case at Re=20,000

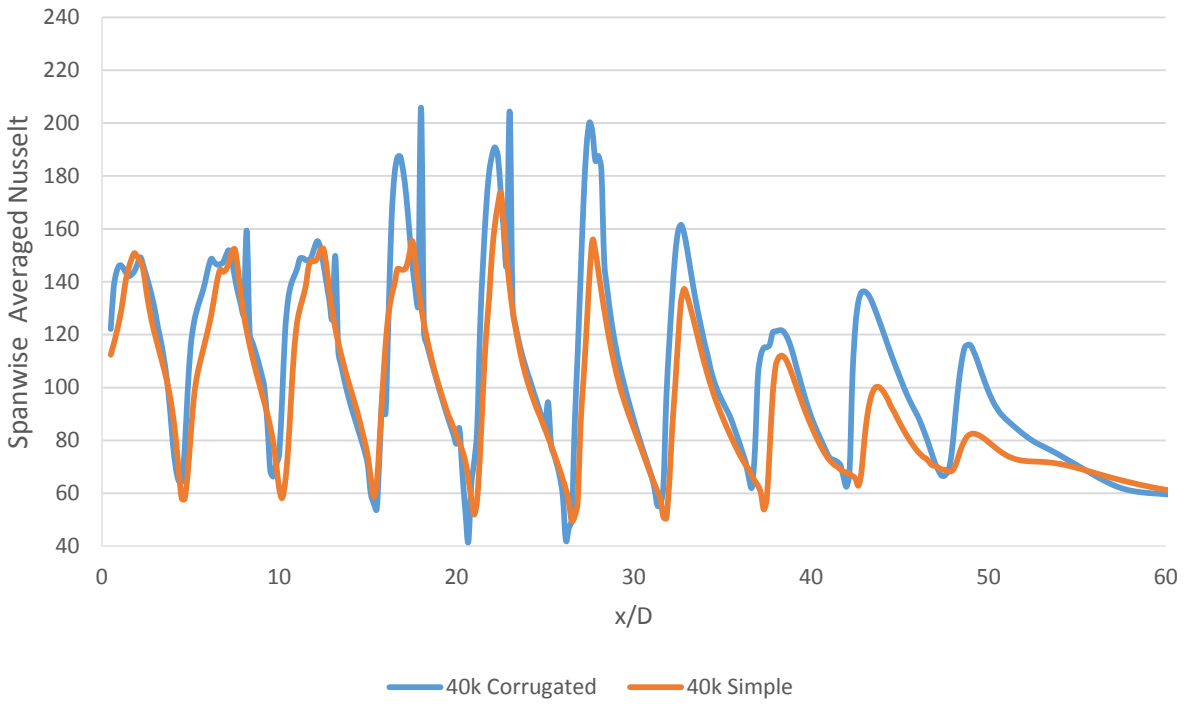

Figure 4.14 – Spanwise averaged Nusselt number for each numerical case at Re=40,000

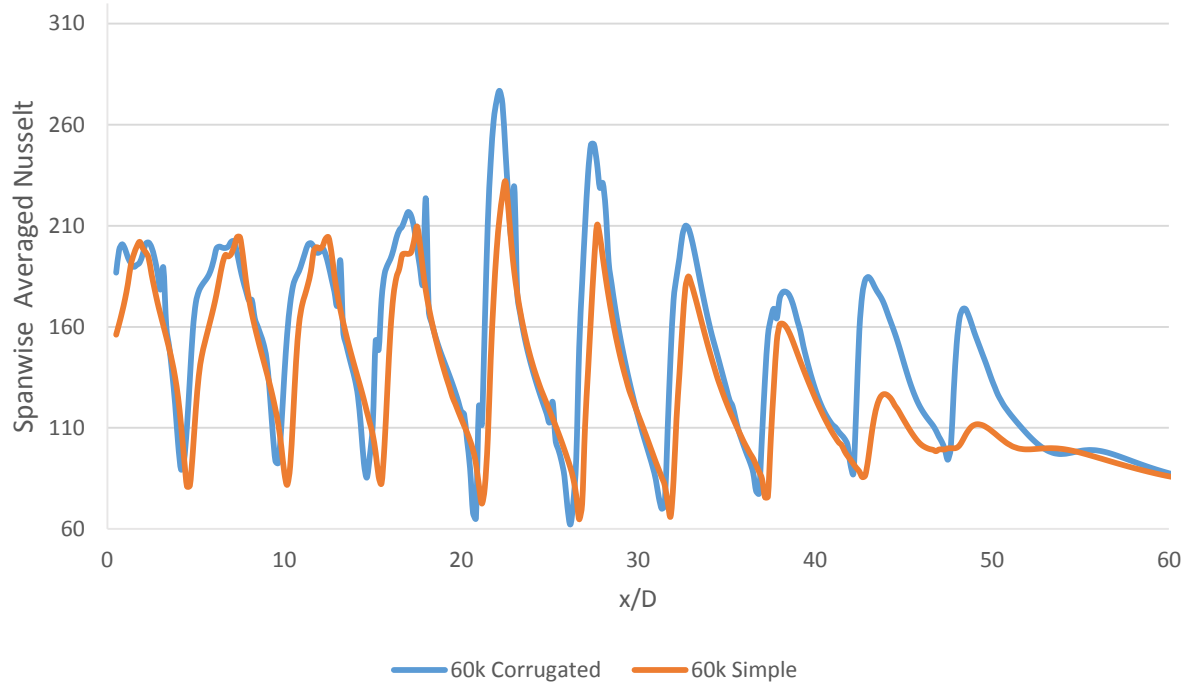

Figure 4.15 – Spanwise averaged Nusselt number for each numerical case at Re=60,000

The experimental values taken directly from [22] can be found in Figure 4.16-18. The extended port and variable extended geometries referred to in the legend were not tested for this study and so can be disregarded (the basic and corrugated geometries are generally the bottom two lines):

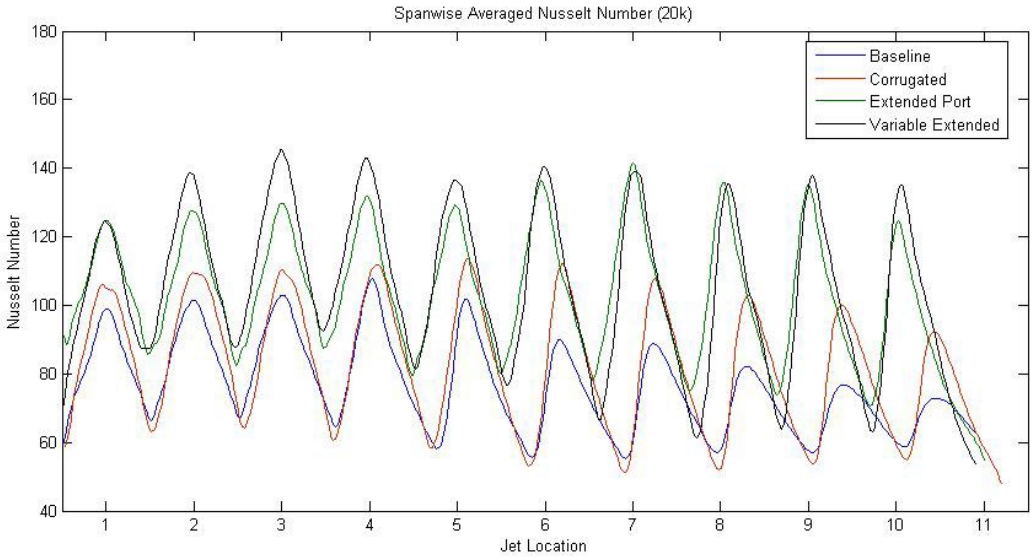

Figure 4.16 – Spanwise averaged Nusselt number for each experimental case at Re=20,000 [22]

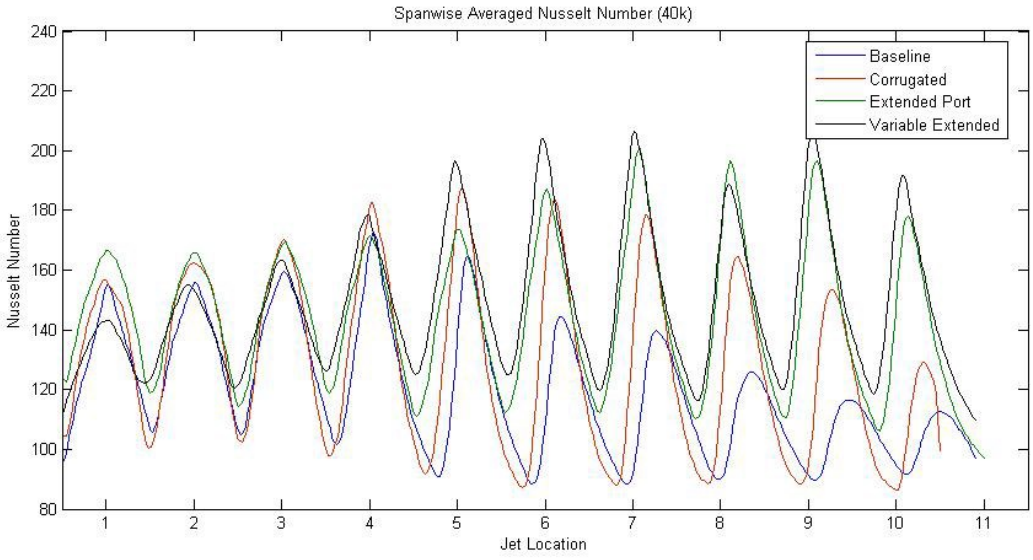

Figure 4.17 – Spanwise averaged Nusselt number for each experimental case at Re=40,000 [22]

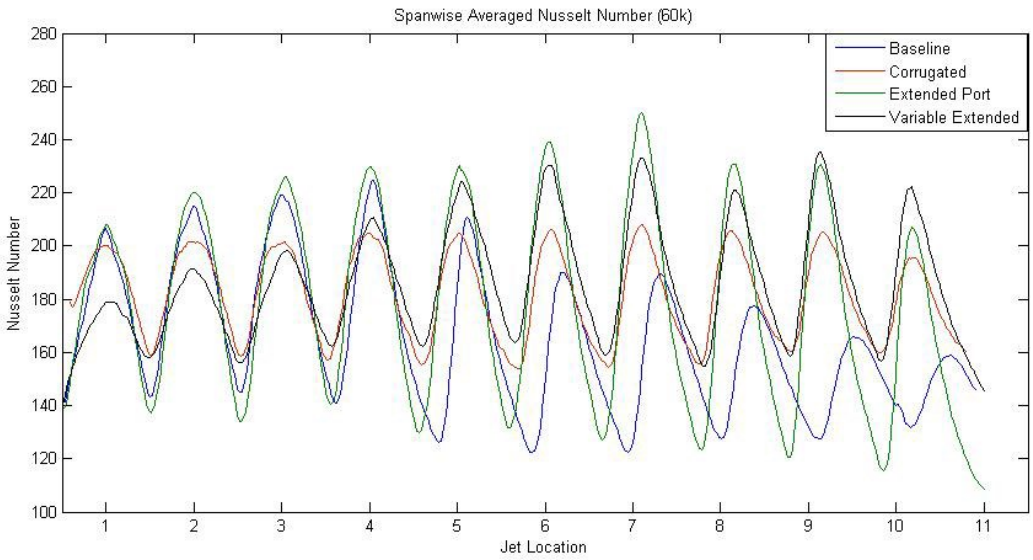

Figure 4.18 – Spanwise averaged Nusselt number for each experimental case at Re=60,000 [22]

The Nusselt number value trends do replicate those of Esposito, with downstream jets benefitting from the corrugations in the geometry. The averaged Nusselt values are roughly the same for the first 3 jets and intervening regions for both geometries, after which the values begin to diverge and the corrugated geometry displays improved performance. The difference is greatest the further downstream the jet and the higher the jet velocity. The purpose of the corrugations is to direct crossflow from upstream jets away from the stagnation region of the downstream jets, therefore improving cooling performance. It can also lead to a reduction in crossflow velocity due to the greater available area. At higher velocities, as jet to jet interactions increase, these benefits would be expected to be enhanced as seen in both the numerical and the experimental results.

Since the experimental results were done without consideration to a numerical validation, it is possible that certain parameters were not exactly replicated, resulting in errors between the two cases. For example, turbulence intensity can significantly affect the local Nusselt values, especially in the stagnation

region. Jensen [54] found that the wall heat flux can rise by up to a factor of 3 for the inlet turbulence intensity changing from 1.5% to 10%. This study was done with a high Reynolds number and an extremely high temperature difference of 1600K where the effects of turbulence on heat transfer are more pronounced, but the effect of intensity on the results is nonetheless highlighted. The overall experimental error was estimated at 8.5%. The discretization error was between 5-10% as mentioned in Chapter 4.2, with up to a further 20% localized error attributed to the model based on the 2D case mentioned in Chapter 3. The jet profile at the inlet was also set to uniform (with a slight amount of development during exit to the chamber), which would not have been strictly true in the experimental case. The results therefore should be accurate in terms of the trends depicted but not necessarily for fully validating the model. Previous works estimate the numerical error at under 10% [52, 55] compared to the experimental values, so any further work must be done in conjunction with the numerical model.

One of the primary aims of CFD is to reduce or even replace experimental work. Since turbulence intensity has been shown to be such a significant factor in heat transfer, it may call into question the validity of any numerical results without experimental work for validation. In this research, turbulence intensity would not have impacted results since both geometries were run at the same inlet intensity and results were merely comparative. However, it is not expected that numerical results can fully replace experimental work at the present time. It may be possible to use experience, correlations and assumptions about flow behavior to make a best guess about velocity profile and inlet intensity to obtain reasonable results in certain numerical models, but without the use of experimental work such results still would not necessarily be adequately rigorous.

The work presented in the previous sections was done without a plenum and with 2 symmetry boundary conditions to reduce computational requirements. This was seen to be a fair approximation of the experimental conditions. Some cases were however also initially run with a plenum and with both a single row and a 1.5 model. The 1.5 model consisted of 1.5 rows of jets, with a symmetry condition through the

middle and a wall on the far side. A plenum with a height of 30 *D* was also placed above the impingement wall. Figure 4.19 below displays the mesh and geometry of the 1.5 model. The single row model simply didn't have the 0.5 row of holes on the side visible in Figure 4.19.

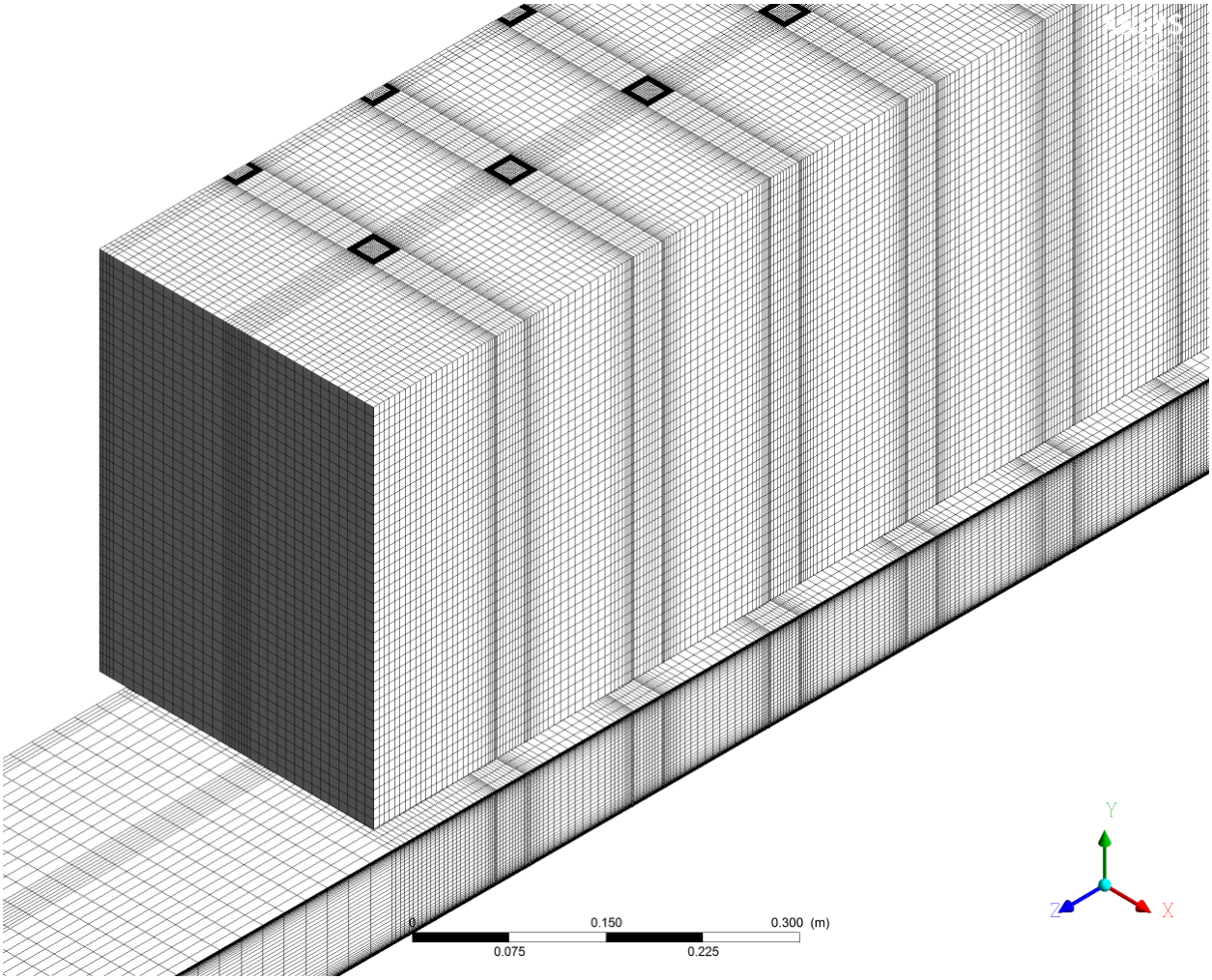

Figure 4.19 – Sample mesh of the 1.5 model

The model was run with the same boundary conditions as the double symmetry model but gave significantly different results. The Nusselt number contours for the 20k Reynolds case in the 1.5 model can be seen in Figure 4.20.

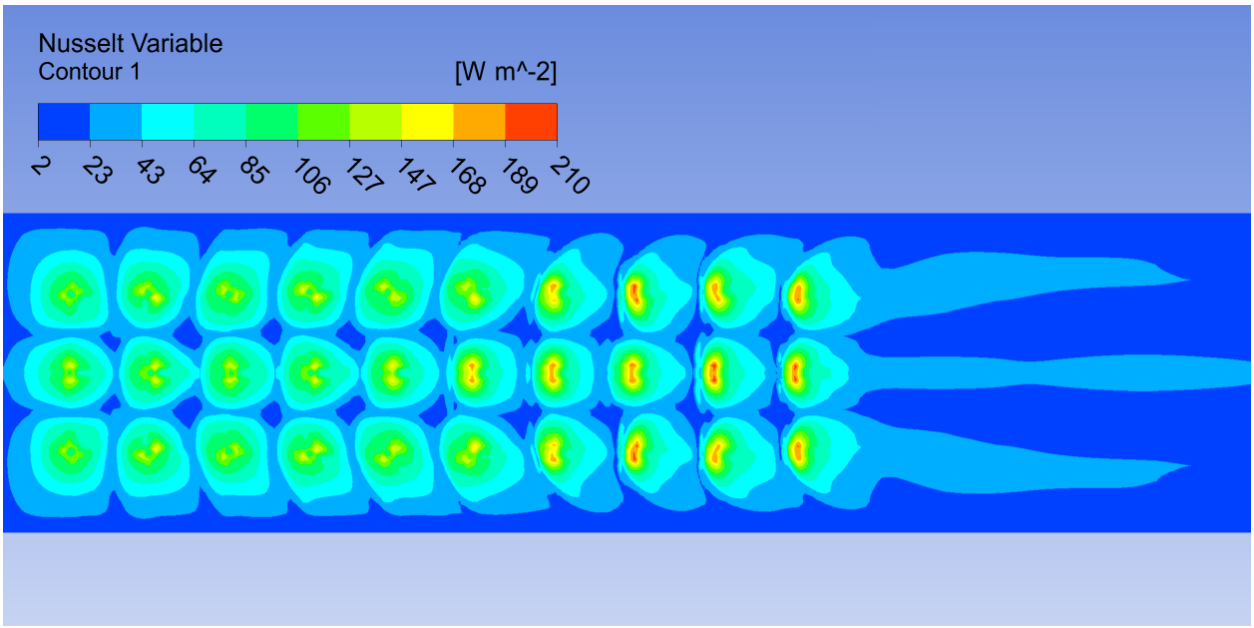

Figure 4.20 – Nusselt contours of 1.5 model with plenum at Re=20,000

In both the single row and the 1.5 model with the plenum, the surface Nusselt number values had error margins exceeding 100%. It was also seen that not only did the Nusselt number degrade downstream, but it actually increased. The plenum velocity inlet was set based on conservation of mass to achieve a Reynolds number of 20k at the pipe exits. This was not strictly maintained however, with the 10th jet approximately 10% faster than the first jet. Since the Nusselt number is proportional to the Reynolds number, an increase in jet velocity would be expected to increase the local Nusselt values. The likely explanation here is that as the crossflow jet velocity increases in the impingement chamber, the associated drop in pressure sucks in a greater amount of air in the downstream jets. This is not borne out in the experiments however, and the effect of a plenum on the computational results should be further investigated.

Chapter 5. CONCLUSIONS AND RECOMMENDATIONS

Two geometries were investigated to assess the suitability of CFD in providing realistic solutions. It was intended to see whether the CFD could replicate the trend seen by the experimental results in that the corrugated geometry offers better cooling performance over large impingement arrays.

It was found through a 2D validation study that the *k-ω* SST model is the most accurate turbulence model for jet impingement cases. The model was then applied to the two geometries.

The same trend as in the experimental results was found with the CFD, with the corrugated geometry showing significantly improved heat transfer characteristics downstream and a negligible impact behind the 4^{th} jet. The corrugations helped both in directing flow away from downstream jets and potentially reducing downstream crossflow velocity due to the greater cross-sectional area available. This effect was only strengthened at higher Reynolds numbers, a trend replicated in both the experimental and the numerical results.

The model could be made more accurate if the experimental results are done with the CFD model in mind. Some parameters including turbulence intensity and the jet profile could not be replicated due to lack of data and issues with the plenum in the numerical model. An initial attempt was made to replicate the velocity profile with a large plenum and different angles of entry for the flow but numerical results deviated significantly from the experimental work. Since these factors can have significant impact on the results, it was impossible to determine exactly the error margin between the two cases. It is however encouraging that the experimental trends were replicated in the numerical results with both geometries being run under identical conditions.

It is suggested that the effect of the plenum and the jet velocity profile on cooling be further investigated, as some researchers mentioned previously have been seen to omit both in recent papers.

REFERENCES

[1] W. Bathie, *Fundamentals of Gas Turbines*, New York: Wiley & Sons, 1984.

[2] J. C. Han, S. Dutta and S. Ekkad, *Gas Turbine Heat Transfer and Cooling Technology*, Boca Raton: CRC Press, 2013.

[3] E. Logan, *Handbook of Turbomachinery*, New York: Marcel Dekker, 2003.

[4] J. Mattingly, W. Heiser and D. Pratt, *Aircraft Engine Design*, Virginia: American Institute of Aeronautics and Astronautics, 2002.

[5] L. Arcangeli, B. Facchini, M. Surace and L. Tarchi, "Correlative analysis of effusion cooling systems," *Journal of Turbomachinery,* vol. 130, pp. 011016.1-011016.7, 2008.

[6] R. Krewinkel, "A review of gas turbine effusion cooling studies," *International Journal of Heat and Mass Transfer,* vol. 66, pp. 706-722, 2013.

[7] G. Cerri, A. Giovannelli, L. Battisti and R. Fedrizzi, "Advances in effusive cooling techniques of gas turbines," *Applied Thermal Engineering,* vol. 27, pp. 692-698, 2007.

[8] N. Zukerman and N. Lior, "Jet impingement heat transfer: Physics, correlations, and numerical modeling," *Advances in Heat Transfer,* vol. 39, pp. 565-639, 2006.

[9] J. Livingood and P. Hrycak, "Impingement heat transfer from turbulent air stream jets to flat plates - A literature survey," *NASA Technical Report,* pp. 1-41, 1973.

[10] H. M. Hofmann, M. Kind and H. Martin, "Measurements on steady state heat transfer and flow structure and new correlations for heat and mass transfer in submerged impinging jets," *International Journal of Heat and Mass Transfer,* vol. 50, p. 3957–3965, 2007.

[11] H. Martin, "Heat and mass transfer between impinging gas jets and solid surfaces.," *Advanced Heat Transfer,* vol. 13, pp. 1-60, 1977.

[12] S. J. Slayzak, R. Viskanta and F. P. Incropera, "Effects of interaction between adjacent free surface planar jets on local heat transfer from the impingement surface," *International Journal of Heat and Mass Transfer,* vol. 37, no. 2, pp. 269-282, 1994.

[13] L. Greers, *Multiple Impinging Jet Arrays: An Experimental Study On Flow And Heat Transfer,* Delft University, Netherlands: PhD Thesis, 2003.

[14] N. Zuckerman and N. Lior, "Radial slot jet impingement flow and heat transfer on a cylindrical target," *Journal of Thermophysics and Heat Transfer,* vol. 21, no. 3, pp. 548-561, 2007.

[15] N. T. Obot and T. A. Trabold, "Impingement heat transfer within arrays of circular jets: Part 1 - Effects of minimum, intermediate, and complete crossflow for small and large spacings," *Heat Transfer,* vol. 109, no. 4, pp. 872-879, 1987.

[16] Y. Xing, S. Spring and B. Weigand, "Experimental and numerical investigation of heat transfer characteristics of inline and staggered arrays of impinging jets," *Journal of Heat Transfer,* vol. 132, p. 092201, 2010.

[17] C. Y. Li and S. V. Garimella, "Prandtl Number effects and generalized correlations for confined and submerged jet impingement," *International Journal of Heat & Mass Transfer,* vol. 44, pp. 3471-3480, 2001.

[18] P. Gulati, Vadiraj Katti and S. Prabhu, "Influence of the shape of the nozzle on local heat transfer distribution between smooth flat surface and impinging air jet," *International Journal of Thermal Sciences,* vol. 48, pp. 602-617, 2009.

[19] J. W. Baughn, A. E. Hechanova and X. Yan, "An experimental study of entrainment effects on the heat transfer from a flat surface to a heated circular impinging jet," *International Journal of Heat and Mass Transfer,* vol. 113, pp. 1023-1025, 1991.

[20] R. J. Goldstein and W. S. Seol, "Heat transfer to a row of impinging circular air jets including the effects of entrainment," *International Journal of Heat Mass Transfer,* vol. 34, no. 8, pp. 2133-2147, 1991.

[21] K. Saunders, S. Alizadeh, L. Lewis and J. Provins, "The use of CFD to generate heat transfer boundary conditions for a rotor-stator cavity in a compressor drum thermal model," *Proceedings of GT07: ASME Turbo Expo,* vol. 4, pp. 1299-1310, 2007.

[22] E. I. Esposito, S. V. Ekkad, Y. Kim and P. Dutta, "Novel jet impingement cooling geometry for combustor liner backside cooling," *Journal of Thermal Science and Engineering Applications,* vol. 1, no. 2, p. 021001, 2009.

[23] K. Anand, *Numerical Heat Transfer Analysis of Micro-Scale Jet Impingement Cooling in a High Pressure Turbine Vane,* Toronto: Ryerson University, Master's Thesis, 2011.

[24] R. P. Williams, T. E. Dyson, D. G. Bogard and S. D. Bradshaw, "Sensitivity of the overall effectiveness to film cooling and internal cooling on a turbine vane suction side," *Journal of Turbomachinery,* vol. 136, pp. 031006-1-7, 2014.

[25] A. Mensch and K. Thole, "Overall effectiveness of a blade endwall with jet impingement and film cooling," *Journal of Engineering for Gas Turbines and Power,* vol. 136, p. 031901, 2014.

[26] D. N. Licu, M. J. Findlay, I. S. Gartshore and M. Salcudean, "Transient heat transfer measurements using a single wide-band liquid crystal test," *Journal of Turbomachinery,* vol. 122, pp. 546-552, 2000.

[27] R. Viskanta, "Heat transfer to impinging isothermal gas and flame jets," *Experimental Thermal and Fluid Science,* vol. 6, no. 2, pp. 111-134, 1993.

[28] K. Ichimiya and N. Hosaka, "Experimental study of heat transfer characteristics due to confined impinging two-dimensional jets," *Experimental Thermal and Fluid Science,* vol. 5, no. 6, p. 803–807, 1992.

[29] D. Lytle and B. W. Webb, "Air jet impingement heat transfer at low nozzle-plate spacings," *International Journal of Heat and Mass Transfer,* vol. 37, no. 12, p. 1687–1697, 1994.

[30] Y. Q. Zu and Y. Y. Yan, "Numerical study on stagnation point heat transfer by jet impingement in a confined narrow gap," *Journal of Heat Transfer,* vol. 131, no. 9, p. 094504, 2009.

[31] K. S. Choo, Y. J. Youn, S. J. Kim and D. H. Lee, "Heat transfer characteristics of a micro-scale impinging slot jet," *International Journal of Heat and Mass Transfer,* vol. 52, pp. 3169-3175, 2009.

[32] L. Huang and M. El-Genk, "Heat transfer of an impinging jet on a flat surface," *International Journal of Heat and Mass Transfer,* vol. 37, pp. 1915-1923, 1994.

[33] R. Gardon and J. C. Akfirat, "The role of turbulence in determining the heat transfer characteristics of impinging jets," *International Journal of Heat Transfer,* vol. 8, pp. 1261-1272, 1965.

[34] T. S. O'Donovan and D. B. Murray, "Jet impingement heat transfer – Part I: Mean and root-mean-square heat transfer and velocity distributions," *International Journal of Heat and Mass Transfer,* vol. 50, pp. 3291-3301, 2007.

[35] C. J. Hoogendorn, "The effect of turbulence on heat transfer at a stagnation point," *International Journal of Heat Transfer,* vol. 20, pp. 1333-1338, 1977.

[36] F. P. Incropera, D. P. DeWitt, T. L. Bergman and A. S. Lavine, *Fundamentals of Heat and Mass Transfer*, Jefferson City: Wiley, 2011.

[37] S. P. Kezios, *Heat Transfer In The Flow Of A Cylindrical Air Jet Normal To An Infinite Plate*, Illinois Institute of Technology, PhD Thesis, 1956.

[38] Y. M. Chung and K. H. Luo, "Unsteady heat transfer analysis of an impinging jet," *ASME Journal of Heat Transfer,* vol. 124, pp. 1039-1048, 2002.

[39] C. Meola, L. De Luca and G. M. Carlomagno, "Influence of shear layer dynamics on impingement heat transfer," *Experimental Thermal Fluids,* vol. 13, pp. 29-37, 1996.

[40] P. J. Roache, "Perspective: A method for uniform reporting of grid refinement studies," *Journal of Fluids Engineering,* vol. 116, pp. 405-413, 1994.

[41] ASME Editorials, "Procedure for estimation and reporting of uncertainty due to discretization in CFD applications," *Journal of Fluids Engineering,* vol. 130, no. 7, p. 078001, 2008.

[42] M. Behnia, S. Parneix and P. Durbin, "Accurate modeling of impinging jet heat transfer," *Center for Turbulence Research Annual Research Briefs,* pp. 149-164, 1997.

[43] F. Menter, J. C. Ferreira, T. Esch and B. Konno, "The SST turbulence model with improved wall treatment for heat transfer predictions in gas turbines," *Proceedings of the International Gas Turbine Congress 2003 Tokyo,* 2003.

[44] F. Menter, "Two-equation eddy-viscosity turbulence models for engineering applications," *AIAA Journal,* vol. 32, no. 8, pp. 1598-1605, 1994.

[45] F. R. Menter, "Review of the shear-stress transport turbulence model experience from an industrial perspective," *International Journal of Computational Fluid Dynamics,* vol. 23, no. 4, pp. 305-316, 2009.

[46] ANSYS Inc, *ANSYS FLUENT 14.5 Theory Guide*, USA, 2012.

[47] J. W. Baughn and S. Shimizu, "Heat transfer measurements from a surface with uniform heat flux and an impinging jet," *Transactions of the ASME,* vol. 111, pp. 1096-1098, 1989.

[48] A. A. Sedlov and V. L. Ivanov, "Numerical simulation of gas dynamics and heat exchange of jet impinging on a surface," *Russian Aeronautics,* vol. 55, no. 4, pp. 75-78, 2012.

[49] D. Singh, B. Premachandran and S. Kohli, "Experimental and numerical investigation of jet impingement cooling of a circular cylinder," *International Journal of Heat and Mass Transfer,* vol. 60, pp. 672-688, 2013.

[50] C. Wan, Y. Rao and P. Chen, "Numerical predictions of jet impingement heat transfer on square pin-fin roughened plates," *Applied Thermal Engineering,* vol. 80, pp. 301-309, 2015.

[51] ANSYS, *ICEM 14.5 User Manual*, 2014.

[52] O. Caggese, G. Gnaegi, G. Hannema, A. Terzis and P. Ott, "Experimental and numerical investigation of a fully confined impingement round jet," *International Journal of Heat and Mass Transfer,* vol. 65, pp. 873-882, 2013.

[53] L. M. Jiji, *Heat Conduction*, New York: Springer, 2009.

[54] M. Jensen and J. H. Walther, "Numerical analysis of jet impingement heat transfer at high jet reynolds number and large temperature difference," *Heat Transfer Engineering,* vol. 34, no. 10, pp. 801-809, 2013.

[55] Z. Chi, R. Kan, J. Ren and H. Jiang, "Experimental and numerical study of the anti-crossflows impingement cooling structure," *International Journal of Heat and Mass Transfer,* vol. 64, pp. 567-580, 2013.

[56] L. Yang, J. Ren, H. Jiang and P. Ligrani, "Experimental and numerical investigation of unsteady impingement cooling within a blade leading edge passage," *International Journal of Heat and Mass Transfer,* vol. 71, pp. 57-68, 2014.

[57] T. J. Craft, L. J. Graham and B. E. Launder, "Impinging jet studies for turbulence model assessment—II. An examination of the performance of four turbulence models," *International Journal of Heat and Mass Transfer,* vol. 36, no. 10, pp. 2685-2697, 1993.

[58] S. J. Wang and A. S. Mujumdar, "A comparative study of five low Reynolds number k–ε models for impingement heat transfer," *Applied Thermal Engineering,* vol. 25, no. 1, pp. 31-44, 2005.

[59] A. El-Jummah, R. A. Husain, G. Andrews and J. Staggs, "Conjugate heat transfer CFD predictions of impingement heat transfer: The influence of hole pitch to diameter ratio x/d at constant impingement gap z," *Proceedings of ASME Turbo expo 2014: Turbine Technical Conference and Exposition,* 2014.

[60] S. Spring, D. Lauffer, B. Weigand and M. Hase, "Experimental and numerical investigation of impingement cooling in a combustor liner heat shield," *Journal of turbomachinery,* vol. 132, no. 1, p. 011003, 2009.

APPENDIX

I. Sample 1 Spanwise Heat Flux Export Script

##The script below describes the generation of one line in the spanwise direction for one of the
##impingement geometries. Once a line is generated, an expression is then made to average a value
##(Nusselt number in this case) on that line, which is then saved as a variable. All the variables are then
##exported out to obtain a plot of the spanwise average of the Nusselt number in the entire geometry.

LINE: Line 1

Apply Instancing Transform = On

Colour = 1, 1, 0

Colour Map = Default Colour Map

Colour Mode = Constant

Colour Scale = Linear

Colour Variable = Pressure

Colour Variable Boundary Values = Conservative

Domain List = /DOMAIN GROUP:All Domains

Instancing Transform = /DEFAULT INSTANCE TRANSFORM:Default Transform

Line Samples = 10

Line Type = Cut

Line Width = 2

Max = 0.0 [Pa]

Min = 0.0 [Pa]

Option = Two Points

Point 1 = -0.15 [m], -0.09 [m], 1.85 [m]

Point 2 = 0 [m], -0.09 [m], 1.85 [m]

Range = Global

OBJECT VIEW TRANSFORM:

Apply Reflection = Off

Apply Rotation = Off

Apply Scale = Off

Apply Translation = Off

Principal Axis = Z

Reflection Plane Option = XY Plane

Rotation Angle = 0.0 [degree]

Rotation Axis From = 0 [m], 0 [m], 0 [m]

Rotation Axis To = 0 [m], 0 [m], 0 [m]

Rotation Axis Type = Principal Axis

Scale Vector = 1 , 1 , 1

Translation Vector = 0 [m], 0 [m], 0 [m]

X = 0.0 [m]

Y = 0.0 [m]

Z = 0.0 [m]

END

END

LIBRARY:

CEL:

EXPRESSIONS:

Line 1 exp =lengthAve(Wall Heat Flux)@ Line 1

END

END

END

EXPRESSION EVALUATOR:

Evaluated Expression = Line 1 exp

END

> forceupdate EXPRESSION EVALUATOR

USER SCALAR VARIABLE: Line 1 variable

Boundary Values = Conservative

Calculate Global Range = Off

Expression = Line 1 exp

Recipe = Expression

Variable to Copy = Pressure

Variable to Gradient = Pressure

END

II. Mesh Sensitivity and GCI values for the 3D Mesh

Corrugated geometry:

Mesh Type	Element Count	Node Count	Average Nusselt Number
Coarse	2,061,256	1,974,760	66.701
Intermediate	4,170,827	4,031,960	67.717
Fine	9,537,120	9,295,536	68.253
Continuum Solution			68.851

Basic Flatplate:

Mesh Type	Element Count	Node Count	Average Nusselt Number
Coarse	1,771,396	1,709,840	63.113
Intermediate	4,049,132	3,941,816	64.869
Fine	8,963,340	9,148,144	66.178
Continuum Solution			70.01

Average Order	**2.438475**
Coarse-Intermediate Relative Error	1.501%

Coarse-Intermediate GCI	2.094%
Intermediate-Fine Relative Error	0.785%
Intermediate-Fine GCI	1.096%
Asymptote check value	1.007915

GCI (Corrugated)

Average Order	**1.120**
Coarse-Intermediate Relative Error	2.708%
Coarse-Intermediate GCI	9.906%
Intermediate-Fine Relative Error	1.978%
Intermediate-Fine GCI	7.237%
Asymptote check value	1.020

GCI (Basic flatplate)